Advanced Remote Sensing Precipitation Input for Improved Runoff Simulation

Local to regional scale modelling

SEYYED HASAN HOSSEINI
WATER RESOURCES ENGINEERING | FACULTY OF ENGINEERING | LUND UNIVERSITY

SEYYED HASAN HOSSEINI obtained a bachelor's degree (2010) in water engineering from the University of Tehran, Iran. He graduated with a master's degree (2013) in water resources engineering from the University of Tabriz, Iran with a thesis about the impact of climate change on streamflow and reservoir operation. He has been working as a researcher on several projects regarding precipitation, climate change, and water resources management in Iran and Sweden since 2012 and 2018, respectively. His affiliation with Lund University started in 2018 as a visiting researcher from the University of Tabriz and then as a PhD student at Lund University, Sweden. He accomplished his PhD thesis about remote sensing of precipitation and data-driven rainfall-runoff modelling at the Faculty of Engineering, Lund University, in 2022.

LUND
UNIVERSITY

Advanced Remote Sensing Precipitation Input
for Improved Runoff Simulation

Advanced Remote Sensing Precipitation Input for Improved Runoff Simulation

Local to regional scale modelling

Seyyed Hasan Hosseini

LUND
UNIVERSITY

Organization	Document name
LUND UNIVERSITY	DOCTORAL THESIS, report TVVR 1095
Department of Building and Environmental Technology	**Date of issue**
Division of Water Resources Engineering	2022 - 06 - 16
Author	Sponsoring organization
Seyyed Hasan Hosseini (Hosseini, S.H.)	
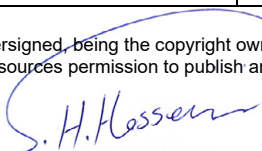
Title and subtitle
Advanced Remote Sensing Precipitation Input for Improved Runoff Simulation – Local to regional scale modelling

Abstract

Accurate precipitation data are crucial for hydrological modelling and rainwater runoff management. Precipitation variability exists through a wide range of spatial and temporal scales and cannot be captured well using sparse rain gauge networks. This limitation is further emphasised for urban and mountainous catchments, especially under global warming, causing an increased frequency of extreme events. Recent advances in remote sensing (RS) techniques make monitoring precipitation possible over larger areas at more regular resolutions than conventional rain gauge networks. The RS data can be biased mainly due to the indirect estimations prone to multiple error sources and temporally discrete observations. The wealth of spatiotemporal precipitation data by RS, however, calls for developing data-driven solutions for both the bias correction and hydrological modelling that, in turn, requires new procedures to assure generalization of the existing methods. The present dissertation comprises a comprehensive summary followed by five appended papers, attempting to evaluate quantitative precipitation estimations (QPE) by state-of-the-art instruments/products for local and regional hydrological applications. Accordingly, two recently installed dual polarimetric doppler X-band weather radars (X-WRs) in southern Sweden and multiple Global Precipitation Mission (GPM) products in Iran were studied at the relevant scales for urban hydrology (1–5-min and sub-km) and large water supply river–reservoir system operation (daily-monthly and 0.1°), respectively. The validation against rain gauge observations (Paper I and II) showed a significant dependency of the X-WR and GPM precipitation errors on the radial distance and regional precipitation pattern, respectively. Taking observations from local tipping bucket rain gauges at the 1–30-km ranges as a reference, the apparent problems with a single X-WR is related to the attenuation during heavy rains and overshooting (at higher elevation angle scans). An internationally bias-corrected GPM product called GPM-IMERG-Final shows a generally good correlation to synoptic observations of over 300 rain gauges in Iran except for extreme observations that are much better predicted by the GPM-IMERG-Late product during spring, summer, and autumn seasons. To leverage the wealth of spatiotemporally complete and validated precipitation data for hydrological modelling, two novel data-driven procedures using artificial neural networks (ANNs) were developed. As in Paper III, the formulation of the new ANN input variables, namely, ECOVs and CCOVs, representing the event- and catchment-specific areal precipitation coverage ratios, improve monthly runoff estimations in all the studied sub-catchments of the Karkheh River basin (KRB) in the mountainous semi-arid climate of western Iran. Merging the doppler and dual-polarization data in the overlapping coverage of the two X-WRs (Paper IV) via an ANN-based QPE improves rainfall detection and accuracy. ANN-assisted estimation of rainfall quantiles, compared to the merging with an empirically based regression model, also shows better results especially related to the extreme 5-min data. Finally, Paper V describes the impact of human activities such as agricultural developments that can equally affect the runoff variation. This fact is considered in Paper III by including MODIS Terra products as additional inputs.

Key words
Artificial intelligence, hydrology, meteorology, precipitation, rainfall, radar, satellite, weather

Classification system and/or index terms (if any)

Supplementary bibliographical information		**Language**
		English

Recipient's notes	**Number of pages**	Price
	214	
	Security classification	

I, the undersigned, being the copyright owner of the abstract of the above-mentioned dissertation, hereby grant to all reference sources permission to publish and disseminate the abstract of the above-mentioned dissertation.

Signature _S. H. Hosseini_   Date 2022-05-19

Advanced Remote Sensing Precipitation Input for Improved Runoff Simulation

Local to regional scale modelling

Seyyed Hasan Hosseini

LUND
UNIVERSITY

Table of Contents

Acknowledgement

First and foremost, I express my profound gratitude to Dr Hossein Hashemi, my main supervisor, and Professor Ronny Berndtsson, my co-supervisor and previous main supervisor, during my PhD at TVRL, the Division of Water Resources Engineering at Lund University (LU). I am grateful for the tremendous experience I achieved by working and finishing my dissertation in their fantastic group. Hossein, your enthusiasm for research discussions and scientific critiques has been exemplary and I highly appreciate all I learned from you and being in your team. Ronny, your unwavering and pure support, given in the most efficient and useful way, as well as your fantastic personality is inimitable and highly appreciated.

My similar appreciation goes to Professor Ahmad Fakheri Fard, my other supervisor at the University of Tabriz (TU), Iran for being a supportive and amazing supervisor.

I also express my gratitude to Dr Khaldoon A. Mourad, my other co-supervisor at LU, and Dr Helen Avery, for giving me the chance to co-author with them a review article about the role of citizen science in environmental and agricultural research during the fantastic time we spent at the Centre for Advanced Middle Eastern studies (CMES), my other affiliation at LU.

CMES sponsored one year of my PhD, among other supports, that I appreciate a lot. I also appreciate all old and new CMES academic and administrative staff for creating a friendly, stimulating, and interdisciplinary research environment.

I appreciate LU innovation's exploratory pre-seed program for funding my project about interdisciplinary radar and AI applications, which helped me broaden my skill and interest in some relatively new areas affected by precipitation. Also, many thanks to Thomas Rundqvist from LU innovation who has generously guided me through the project regarding collaboration with industry, among other things.

I am also grateful for the opportunity to collaborate with a well-knit team of researchers and stakeholders active in developing Sweden's first X-band weather radar network during my PhD. Many thanks to Dr Rolf Larsson, an admirable mentor and Associate Professor at TVRL, Professor Jonas Olsson, research leader at SMHI and Adjunct Professor at TVRL, Professor Henrik Aspegren, CEO of Sweden Water Research and Adjunct Professor at LU, Dr Remco van de Beek, senior researcher at SMHI, Sven Bengtsson from NSVA, Simon Granath from VA Syd, Nicholas South from Tyréns as well as their other team members involved in the Svenskt Vatten projects, among other invaluable collaborations since 2018.

At TVRL, I would like to extend my appreciation to Professor Magnus Larson for being a major support by showing willingness to discuss various educational and research questions with his broad knowledge and friendly behaviour; Professor Kenneth Persson, for his esteemed leadership and winning mindset, among his other fantastic personalities, that everyone wishes to have in their organization; Görel

<div align="right">
Seyyed Hasan Hosseini

Lund, 2022-May-19
</div>

Popular Science Summary

The journey of water over land gets more exciting when it rains. The rainwater accumulates over surfaces, penetrates the soil, leaches substances, and runs off in rivers until it ends at larger water bodies or evaporates into the air. Studying these precipitation effects is essential for the successful management of water availability and hazard problems such as water supply and flood control.

The performance of computer tools used by hydrologists for runoff simulation largely relies on the accuracy of the precipitation data. As transient and severe as cloudbursts, precipitation can be highly variable across time and area. Rain gauge stations that measure precipitation at a point scale cannot represent the areal precipitation properly if they are not distributed and maintained well in a drainage area. In the last decades, remote sensing by centralized instruments such as satellite sensors or ground-based weather radars provides a wealth of precipitation data in larger areas and more regular resolutions than a usual rain gauge network does. Due to the indirect estimations by remote sensing, most of the recent studies focused on the validation and bias correction of the remote sensing data.

This dissertation, mainly based on the appended papers I-IV, investigates the recent advances in remote sensing of precipitation at scales that are relevant to urban and regional scale runoff simulation. Paper V is additionally appended to discuss the importance of other remote sensing data such as evaporation and vegetation in runoff simulation.

Primarily, the ground validation against rain gauge observations was performed for three daily and one monthly precipitation product at grids of about 10-km size from the Global Precipitation Mission (GPM) of NASA over Iran (Paper I) as well as for the sub-kilometre and minute scale precipitation data from Sweden's first dual-polarization Doppler X-band weather radar (Paper II). These studies reviewed the literature and theoretical backgrounds and highlighted the challenges regarding the future application as well that were partly addressed in Papers III and IV.

The spatially distributed remote sensing data are mostly used in conceptually based computer models. These models can be structurally and computationally expensive due to their complex input requirements and procedures. The computationally advanced data-driven models based on artificial intelligence (AI) can promote efficient alternatives. But, without using physical equations, AI models require additional methods to assure a generalized solution regardless of the parsimonious approach. Artificial Neural Networks (ANNs) are among the most popular types of AI-assisted data-driven models in hydrology that are used in this dissertation for two purposes:

- Developing novel remote sensing data-driven solutions for regional-scale monthly runoff simulation to enhance surface water management in data-scarce regions (Paper III).

- Merging local X-band weather radars for consistent high-resolution rainfall estimation to advance stormwater monitoring and management in urban areas (Paper IV).

In Paper III, five mountainous drainage areas of the Karkheh River in western Iran were studied. The satellite precipitation data were formulated in form of a few novel inputs to the ANN that resulted in obvious improvement of runoff simulations in all the areas. However, areas with higher spatiotemporal variability of precipitation showed a higher need for longer satellite records.

In Paper IV, single and merged radar rainfall estimates in the overlapping coverage area of the two X-band weather radars were evaluated against the records of 38 rain gauges. The validated data indicated better performance of the ANN compared to the regression-based combination of traditional empirical methods, especially for the severe rainfall values.

Paper V showed that human activities could be as important as climate factors in runoff variation. In the catchments with agricultural development, the human effects could be partially considered by monitoring vegetation and evaporation via remote sensing. Paper III included such supplementary data based on the MODIS satellite observations along with the GPM precipitation in monthly runoff simulations useful for water supply planning.

In conclusion, the combination of remote sensing and AI-assisted data-driven solutions seems promising for coping with the rainwater-related challenges where gauge measurements are lacking or limited. As a result of improved precipitation and runoff data for urban and rural planners, liveability can then be promoted.

Abstract

Accurate precipitation data are crucial for hydrological modelling and rainwater runoff management. Precipitation variability exists through a wide range of spatial and temporal scales and cannot be captured well using sparse rain gauge networks. This limitation is further emphasised for urban and mountainous catchments, especially under global warming, causing an increased frequency of extreme events. Recent advances in remote sensing (RS) techniques make monitoring precipitation possible over larger areas at more regular resolutions than conventional rain gauge networks. The RS data can be biased mainly due to the indirect estimations prone to multiple error sources and temporally discrete observations. The wealth of spatiotemporal precipitation data by RS, however, calls for developing data-driven solutions for both the bias correction and hydrological modelling that, in turn, requires new procedures to assure generalization of the existing methods. The present dissertation comprises a comprehensive summary followed by five appended papers, attempting to evaluate quantitative precipitation estimations (QPE) by state-of-the-art instruments/products for local and regional hydrological applications. Accordingly, two recently installed dual polarimetric doppler X-band weather radars (X-WRs) in southern Sweden and multiple Global Precipitation Mission (GPM) products in Iran were studied at the relevant scales for urban hydrology (1–5-min and sub-km) and large water supply river–reservoir system operation (daily-monthly and 0.1°), respectively. The validation against rain gauge observations (Paper I and II) showed a significant dependency of the X-WR and GPM precipitation errors on the radial distance and regional precipitation pattern, respectively. Taking observations from local tipping bucket rain gauges at the 1–30-km ranges as a reference, the apparent problems with a single X-WR is related to the attenuation during heavy rains and overshooting (at higher elevation angle scans). An internationally bias-corrected GPM product called GPM-IMERG-Final shows a generally good correlation to synoptic observations of over 300 rain gauges in Iran except for extreme observations that are much better predicted by the GPM-IMERG-Late product during spring, summer, and autumn seasons. To leverage the wealth of spatiotemporally complete and validated precipitation data for hydrological modelling, two novel data-driven procedures using artificial neural networks (ANNs) were developed. As in Paper III, the formulation of the new ANN input variables, namely, ECOVs and CCOVs, representing the event- and catchment-specific areal precipitation coverage ratios, improve monthly runoff estimations in all the studied sub-catchments of the Karkheh River basin (KRB) in the mountainous semi-arid climate of western Iran. Merging the doppler and dual-polarization data in the overlapping coverage of the two X-WRs (Paper IV) via an ANN-based QPE improves rainfall detection and accuracy. ANN-assisted estimation of rainfall quantiles, compared to the merging with an empirically based regression model, also shows better results especially related to the extreme 5-min data. Finally, Paper V describes the impact of human activities such as agricultural

developments that can equally affect the runoff variation. This fact is considered in Paper III by including MODIS Terra products as additional inputs.

Papers

List of appended papers

I. Maghsood F. F., Hashemi H., **Hosseini S. H.** & Berndtsson R. 2020. "Ground validation of GPM IMERG precipitation products over Iran", Remote Sensing, 12(1), 48. https://doi.org/10.3390/rs12010048

II. **Hosseini S. H.**, Hashemi H., Berndtsson R., South N., Aspegren H., Larsson R., Olsson J., Persson A. & Olsson L. 2020. "Evaluation of a new X-band weather radar for operational use in south Sweden", Water Science and Technology, 81(8): 1623–1635. https://doi.org/10.2166/wst.2020.066

III. **Hosseini S. H.**, Hashemi H., Fakheri Fard A. & Berndtsson R. 2022. "Areal Precipitation Coverage Ratio for Enhanced AI Modelling of Monthly Runoff: A New Satellite Data-Driven Scheme for Semi-Arid Mountainous Climate". Remote Sensing, 14(2), 270. https://doi.org/10.3390/rs14020270

IV. **Hosseini S. H.**, Hashemi H., Larsson, R., Berndtsson R. "Merging dual-polarization X-band radar network intelligence for improved microscale observation of summer rainfall in south Sweden". (submitted).

V. Kazemi H., Hashemi H., Maghsood F., **Hosseini S. H.**, Sarukkalige R., Jamali S. & Berndtsson R. 2021. "Climate vs. Human Impact: Quantitative and Qualitative Assessment of Streamflow Variation", Water, 13 (17), 2404. https://doi.org/10.3390/w13172404

Author's contributions to the appended papers

I.   The author (SHH) contributed equally to the paper (including planning, discussing, and writing efforts) as the first and the second authors did and he was the corresponding author. For the executions, the second author supervised the procedure. The first author collected the remote sensing data and plotted the GIS maps. SHH collected gauge data, conducted all the gauge-satellite data comparisons using statistical criteria, and provided all the tabular (including those used in the maps) and most of the graphical results and discussions about them. The fourth author contributed mostly to the technical reviewing and revising.

II.   SHH was the leading and corresponding author. He planned the research and discussed the results with the co-authors. He conducted the research and prepared all the initial and revision drafts including all sections and illustrations.

III.   SHH was the leading and corresponding author. He planned and conducted the research and prepared all the initial and revision drafts including all sections and illustrations. All authors contributed by discussing the results and revising the drafts.

IV.   SHH was the leading and corresponding author. He planned the research and discussed the results with the co-authors. He conducted the research and prepared all the drafts including all sections and illustrations. All authors contributed by revising the drafts.

V.   The underlying research was about runoff variations at the same catchment as in paper III but with a different approach. SHH contributed to the data analyses, methodology, and writing (reviewing and editing) together with the first author and other co-authors.

Supporting Publications and Conference Presentations

Peer-reviewed journal

- Boroughani M., Hashemi H., **Hosseini S. H.**, Pourhashemi S. & Berndtsson R. 2020. "Desiccating Lake Urmia: A New Dust Source of Regional Importance". IEEE Geoscience and Remote Sensing Letters, 17(9): 1483-1487. https://doi.org/10.1109/LGRS.2019.2949132

- Mourad K.A., **Hosseini S. H.** & Avery H. 2020. "The Role of Citizen Science in Sustainable Agriculture". Sustainability, 12(24), 10375.

  https://doi.org/10.3390/su122410375

Specialist publication article

- **Hosseini S. H.** 2019. Disastrous Floods after Prolonged Droughts Have Challenged Iran. FUF-Bladet (The Swedish Development Forum), pp. 30–32.
  https://portal.research.lu.se/en/publications/disastrous-floods-after-prolonged-droughts-have-challenged-iran

Technical report

- South N., Hashemi H., Olsson L., **Hosseini S. H.**, Aspegren H., Larsson R., Berndtsson R., Das R., Marmbrandt A. Olsson J. & Persson A. (2019). Väderradarteknik Inom VA-Området: Test av Metodik. Rapport 2019-3, Svenskt Vatten Utveckling, Sweden. (In Swedish).
  https://portal.research.lu.se/en/publications/weather-radar-technology-within-water-and-wastewater-treatment-te

Conference Presentations

- **Hosseini S.H.**, Hashemi H., Berndtsson R., Larsson R., South N. & Aspegren H. (accepted extended abstract for oral presentation in 2020). X-band weather Radar Error in High-Resolution Extreme Rainfall Monitoring: Improvement Possibilities. IWA World Water Congress & Exhibition, Copenhagen, Denmark. Postponed to September 2022.

- **Hosseini S. H.**, Hashemi H., Berndtsson R., South N., Aspegren H., Larsson R., Olsson J., Persson A., Olsson L. & Marmbrandt A. (2019). Evaluation of a new X-band weather radar – experiences from Sweden. WaterMatex2019, Copenhagen, Denmark. 1-4 Sep 2019.

- Hashemi H., **Hosseini S. H.**, Maghsood F. D. (2019). Ground validation of GPM IMERG rainfall products over Iran country. AGU Fall meeting, American Geophysical Union, abstract #H31P-1993. 9-13 Dec 2019.

Abbreviations

ANN	Artificial Neural Network (here, used for monthly runoff modelling or merging of X-WR data)
CC	Correlation Coefficient (here, equivalent to PCC)
DBZH	Horizontal reflectivity in dB (an X-band WR variable)
FAR	False Alarm Ratio
GPM	Global Precipitation Mission (an international program led jointly by NASA and JAXA)
GSS	Gilbert Skill Score
IMERG	Integrated Multi-satellitE Retrievals for GPM
IPCC	The United Nations' Intergovernmental Panel on Climate Change
JAXA	The Japan Aerospace Exploration Agency
KDP	Specific differential phase in degrees km^{-1} (an X-band WR variable)
KGE	King-Gupta Efficiency
KRB	Karkheh River Basin
MAE	Mean Absolute Error
MODIS	Moderate Resolution Imaging Spectroradiometer (a key instrument on Terra and Aqua satellites)
MSE	Mean Squared Error
NASA	The National Aeronautics and Space Administration of the U.S. federal government
NSE	Nash-Sutcliffe Efficiency
NSVA	Nordvästra Skånes Vatten och Avlopp (a water utility company in southern Sweden)
PCC	Pearson Correlation Coefficient
PHIDP	Differential phase (an X-band WR variable)
POD	Probability of Detection
QPE	Quantitative Precipitation Estimation
RAE	Relative Absolute Error
RATE	Rainfall rate in mm h^{-1} (an X-band WR product)

rBIAS   Relative Bias

RHOHV   Correlation between horizontal and vertical reflectivity, variable (an X-band WR variable)

RMP   A linear regression model used for merging X-band WR rainfall products (RATEs)

RS   Remote Sensing

SMHI   Swedish Meteorological and Hydrological Institute

WR   Weather Radar

VA Syd   A water utility company in southern Sweden

VRAD   Radial velocity in m s^{-1} (an X-band WR variable)

ZDR   Logged differential reflectivity between horizontal and vertical in dB (an X-band WR variable)

1 Introduction

1.1 Problem Statement

Variability is a key characteristic of precipitation making it interesting for many scientists to study. Some climates receive more precipitation than others but heavy rainstorms with devastating effects often occur in arid to semi-arid climates (Hosseini, 2019). Similarly, droughts that are more frequent in drier climates are not uncommon in humid regions. The impacts of global warming in the past decades correlate with a higher frequency of these extreme events (Myhre et al., 2019; Tabari, 2020) or lack of precipitation. For example, 2018 and 2019 included the first consecutive drought in more than 250 years in central Europe (Hari et al., 2020). It was estimated that the heavy precipitation, droughts, and heatwaves caused about € 487 billion of economic losses during the 1980-2020 period, equivalent to 80% of the total losses of natural hazards, in Europe[1]. In some arid to semi-arid regions, e.g., in Iran, it appears that the "normal" hydrological conditions are changing and flood and drought events are increasing (Hosseini, 2019).

Precipitation data in hydrology are often used for runoff modelling, usually concerning surface water availability and hazard problems. Precipitation data must represent the spatial and temporal variability well to accurately estimate the corresponding runoff variations over time at the desired time scale. Otherwise, the uncertainty of precipitation misrepresentation to runoff simulation can put engineering decisions such as water supply and flood control on shaky ground. According to the definitions in Orlanski (1975) for the space and time scales of the meteorological processes, precipitation events can appear among a broad range of horizontal space including Micro γ (e.g., tornadoes and deep convection at 0.2-2 km), Meso α (e.g., thunderstorms at 2-20 km), Meso β (e.g., squall lines and cloud cluster at 20-200 km) and Meso γ (e.g., fronts at 200-1000 km) scales with the equivalent characteristic time of a few minutes to an hour, one to a few hours, a few hours to a day, and a day to a few weeks, respectively. The predictions of more

---

[1] https://www.eea.europa.eu/data-and-maps/figures/economic-damage-caused-by-weather-5/

extreme events around the globe by the Intergovernmental Panel on Climate Change (IPCC) can be translated to even higher variability of precipitation for the catchments as the nature of many extreme events is connected to convection (Moustakis et al., 2020).

In view of the above, precipitation monitoring at high spatiotemporal resolution is necessary for developing better hydrologic models dealing with the contemporary and future climate. It is, however, noted that the required resolution depends on the hydrological problem and the catchment's characteristics. Due to orographic and urbanisation impacts on local to regional scale precipitation (Furcolo et al., 2016; Houze, 2012; Liu and Niyogi, 2019; Yang and Ren, 2022) as well as the substantially diverse runoff response in complex terrains and heterogenous urban surfaces, high-resolution precipitation data are of most interest in catchments with such characteristics. Temporally, large water supply river-reservoir systems can operate on the weekly to seasonal aggregations of rainfall data while resolutions as short as 1-5 minutes are necessary for urban flood prediction. Spatially, a range of convective to orographic effects that can result in severe precipitation events at local to regional scales may have different importance depending on the catchment size. Using the definitions noted earlier, the recommended data scales could be summarized as Micro γ and Meso α for urban and rural catchments, respectively. Nevertheless, these scales should not neglect the smaller-scale dynamics. Hence, the actual observations can be ideally collected from even smaller scales but be summed up to the desired scale for the hydrological models.

Precipitation data scarcity is a terminology used for explaining the lack of information about precipitation either related to the low-resolution observations or short length of records. The traditional measurements of precipitation via in-situ rain gauges are usually available for longer periods. However, their efficacy is largely limited by the extensive infrastructural, technological, and financial requirements regarding the regular installation and maintenance of sufficiently dense gauge networks operating at suitable temporal aggregation. As discussed above, this limitation is most relevant for urban and mountainous catchments. Remote sensing (RS) of precipitation using satellites and ground-based weather radars (WRs), as an alternative or supplement to the gauge networks, are among the promising tools for meeting the micro to meso-scale demands regarding precipitation observations. Usually, it is not only the spatiotemporal resolution but also the areal coverage of the observations that can be improved by RS.

Due to the indirect estimations, and temporally discrete sampling by RS, however, they can carry a variable degree of uncertainty that should be addressed. The validation of the RS data is not always straightforward due to the incomparable scale and nature of the gauge–RS observations. With advanced computational techniques such as artificial intelligence, it is assumed that the wealth of spatiotemporal data can be used to advance hydrological calculations. This assumption, however, needs significant analyses and unbiased validations. This dissertation attempts to address

the necessity and challenges of RS precipitation and develop new satellite and X-band WR (X-WR) data-driven solutions for hydrological applications.

1.2 Objectives and Structure

Given the problems concerning precipitation data scarcity at local to regional scales and the potential for improving RS solutions using computationally advanced data-driven procedures, this section summarises the aims and objectives of the dissertation followed by an overview of the structure of the dissertation.

1.2.1 Aims and objectives

Two main aims of the dissertation were:

- Ground validation of the state-of-the-art RS precipitation data for local and regional scale hydrological applications

- Improvement of quantitative precipitation estimation (QPE) for urban and rural runoff simulations by developing RS data-driven procedures

Each of the above aims was pursued with two studies focusing on the two highest available resolution precipitation observations using local WRs and global satellites for urban and rural applications, respectively.

The main objectives were:

- Investigating the accuracy of precipitation monitoring using satellite products and local X-WR by ground validation using rain gauges at different scales (Papers I and II)

- Formulating new satellite-based inputs for a better explanation of areal precipitation variability using a generalized ANN-based precipitation–runoff simulation model (Paper III)

- Addressing inconsistent single X-WR-based QPE by developing new data-driven merging models combining multiple-level measurements of a composite of two X-WRs, resulting in regular grid products (Paper IV)

- Distinguishing human from climate impacts on large river flow variations using theoretical approaches and validations by RS and hydrological modelling (Paper V)

1.2.2 Dissertation structure

As shown in Figure 1, the dissertation is structured based on four main papers (Papers I-IV) and an additional one (Paper V) as a supplementary for Paper III. Papers I-IV are related in two ways based on the RS data source (satellite or WR) and whether the focus was on ground validation via rain gauges or modelling new RS data driven procedures using ANN modelling.
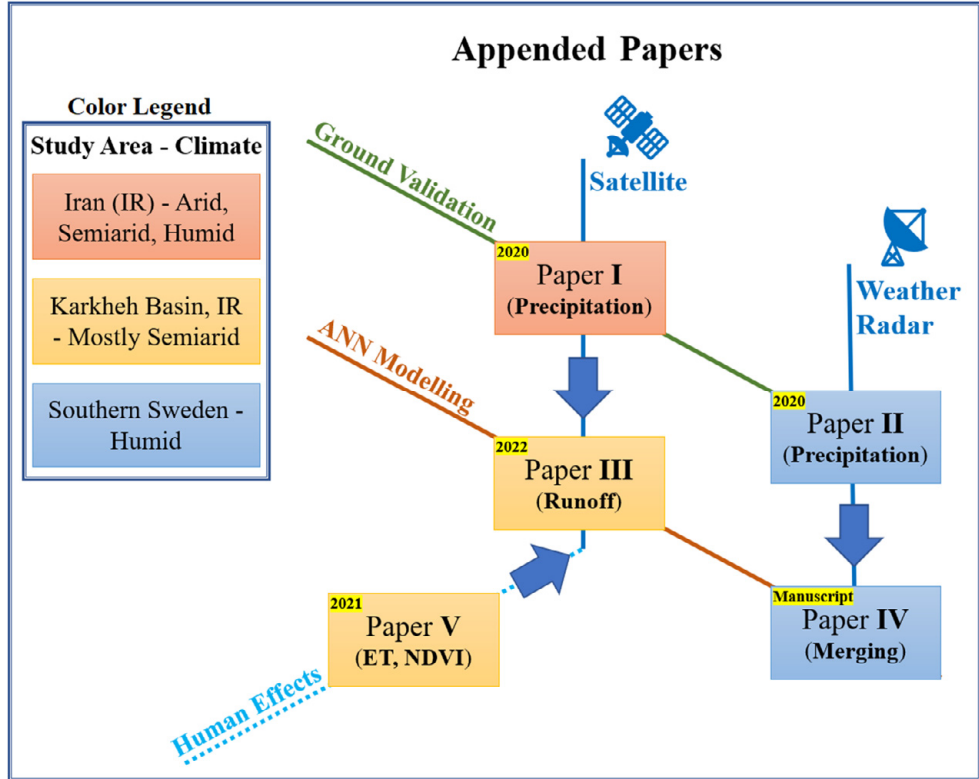
Figure 1. Diagram of the five appended papers (Papers I-V) illustrating the publication year, a descriptive keyword, and the study area and climate according to the legend (blue for southern Sweden and orange and red for Karkheh River Basin in Iran and the entire Iran country, respectively). The first four papers (Paper I-IV) are related in two ways; first, the underlying RS data sources ("Satellite" and "Weather Radar"); and, second; by "Ground Validation" and "ANN Modelling" that emphasise the methodology. As shown with the arrows, Paper III relied on the first and fifth papers (Papers I and V), and Paper IV relied on Paper II.

The papers were based on two relevant case studies from Sweden and Iran where precipitation data scarcity was important for urban and rural applications, respectively. More accurately, for the ground validation studies, sub-km and minute rainfall estimations of an X-WR at 1–30-km radius were studied in southern Sweden while daily and monthly satellite precipitation products at approximate grid sizes of 9 km × 11 km from Global Precipitation Mission (GPM) across the entire Iran

country were used. In addition, for the improved RS data-driven solutions (using ANN modelling), the case study in Sweden covered the overlapping area of two X-WRs at their maximum range coverage radius of 50 and 70 km in south Sweden while the case study in Iran included five mountainous catchment areas of the large Karkheh River Basin (KRB) in western Iran.

2 Literature Review

2.1 Satellite Precipitation

2.1.1 Introduction

Accurate precipitation data are fundamental to evaluating water availability and hazards regarding hydrological applications (Xu et al., 2015, Liu et al., 2017, Sun et al., 2018). Precipitation can either be directly measured on the ground by rain-gauge or be indirectly estimated aloft using RS techniques such as ground-based WR and satellite-based instruments. Rain gauges traditionally provide a reliable dataset used for most of studies at the hydrological catchment scales. However, they may not properly reflect the areal rainfall variability depending on the density of the rain gauge network and the complexity of rainfall (Hiebl and Frei, 2018). The alternative estimation of precipitation can be obtained by ground-based WRs but may suffer from error sources such as ground clutter, wet radome attenuation, rain-induced attenuation, and non-uniform beam filling (Van de Beek et al., 2016). Moreover, several reasons such as incomplete areal coverage especially over oceanic and sparsely populated areas (Rana et al., 2015; Kidd et al., 2017), along with the lack of an integrated system for reporting ground-based observations in many regions (Omranian and Sharif, 2018) make them insufficient for larger-scale studies. These limitations need to be addressed considering the holistic view of environmental processes in relation to the climate change studies as well as to the long-term weather forecast applications. With advanced instruments, satellite observations compensate for these deficiencies by providing more spatially homogeneous and temporally complete coverage for the vast majority of the globe (Kidd and Levizzani, 2011; Sun et al., 2018).

2.1.2 Precipitation products

There are various global scale satellite-based precipitation products at multiple temporal and spatial resolutions that are freely available to the public or academia, out of which the Global Precipitation Measurement (GPM) (Hou et al., 2014), Tropical Rainfall Measuring Mission (TRMM) (Huffman et al., 2007), Precipitation Estimation from Remotely Sensed Information using Artificial Neural Networks

(PERSIANN) (Hsu et al., 1997), and Climate Prediction Center Morphing (CMORPH) (Joyce et al., 2004) are the most widespread ones. As one of the most recent missions, the GPM core observatory was launched in February 2014, as a successor to the TRMM, to continue and improve satellite-based precipitation observations globally. Using the algorithms underlying in TRMM-Multi-Satellite Precipitation Analysis (TMPA), PERSIANN-Cloud Classification System, PERSIANN-CCS) estimates, and CMORPH-Kalman Filter (CMORPH-KF) time interpolation scheme, the Integrated Multi-satellite Retrievals for GPM (IMERG) combines the collected information from the satellites' passive microwave (PMW) and microwave-calibrated infrared (IR), and precipitation-gauge analyses (for regionalization and bias correction), into half-hourly 0.1º×0.1º gridded fields (Huffman et al., 2015; Huffman et al., 2019). The morphing process, integrating geostationary infrared satellites for filling the gap between the intermittent microwave observations by the satellite constellation for GPM, is the way IMERG algorithm addresses the temporally discrete observations. The IMERG algorithm is now run for both TRMM and GPM eras (since 2000; Huffman et al., 2019) and produce multiple products at different latency going back to 2000 (Paper III).

A search in Web of Science exemplies that GPM and its precursor products comprised roughly one-third (=398/1239) of the publications regarding satellite precipitation in the context of hydrology during the past few years (2018-2021). The detail of the search is summarised in Table 1 (TI, AB, and TS show that the keywords were specifically searched in the title, abstract, and topic, respectively. AND, and OR are Boolean operators and * represents any group of characters):

Table 1. Web of Science search results showing the importance and interest of GPM and TRMM and their corresponding algorithms IMERG and TMPA in the hydrology literature.

Search phrase	Years	Number of results
(TI=(satellite AND (precipitation OR rain*)) OR AB=(satellite AND (precipitation OR rain*)) AND TS=(hydrolog*)	2018 – 2021	1239
(TI=(satellite AND (precipitation OR rain*) AND **(GPM OR IMERG OR TRMM OR TMPA)**) OR AB=(satellite AND (precipitation OR rain*) AND **(GPM OR IMERG OR TRMM OR TMPA)**)) AND TS=(hydrolog*)	2018 – 2021	398

2.1.3   Challenges and approaches

Satellite precipitation is subject to some significant uncertainties mostly including estimation through cloud top reflectance, thermal radiance, infrequent satellite overpasses and algorithm, which originate due to their indirect nature (Khodadoust Siuki et al., 2017). Hence, a preliminary validation of satellite precipitation data in each specific region can be helpful to promote improvement in processes of satellite rainfall retrieval as well as for users in different applications (Tan and Santo, 2018). Along this line, extensive studies have been allocated to the evaluation of IMERG estimates compared to ground observations of rainfall such as radars and gauges or other existing satellite datasets in different parts of the world (e.g., Roca et al., 2010;

Chen et al., 2013; Hashemi et al., 2017; Worqlul et al., 2014; Sun et al., 2018; Mondal et al., 2018).

Even though gauge data are the ground reference in many of these studies, it should be noticed that gauge measurements are also subject to uncertainties (Villarini et al., 2008), especially in terms of areal representativeness compared to the relatively coarse grids of satellite data, and wind-induced under catch. In this sense, the ground validation studies are mainly applying two major approaches depending on the form of the available reference data. Some compare the point data from the gauges to the satellite grid (point-to-grid), while the others use the spatially interpolated ground data in form of regular grids as reference (grid-to-grid).

Gridded precipitation datasets offer a solution to the problems of missing data and spatial bias resulting from uneven or unrepresentative spatial measurements, although not a perfect solution (Ensor and Robeson, 2008). The reliability of the interpolated precipitation can depend on the density of the in-situ measurements and the nature of the rainfall, which is variable by time and geospatial heterogeneity. While some developing countries suffer from acute data shortage, both in terms of quality and quantity of measurements (Beria et al., 2017), there are some successful examples of evaluations based on quite dense rain-gauge networks such as the ones used by Foelsche et al. (2017), and Omranian and Sharif, (2018). A problem appears when there is no access to such a dense network in many areas of the world. While the interpolation of rather sparse in-situ data does not result in a substantial problem for monthly or annual time scales (Ensor and Robeson, 2008), some studies show that the routinely used interpolation methods (e.g., ordinary kriging, and inverse distance weighting) in the ground validation studies can produce datasets with significantly different statistical characteristics compared to the original observations (Ensor and Robeson, 2008; Wagner et al., 2012). The interpolation can decrease the spatial variability of precipitation (Xu et al., 2015), making them less valid methods. To improve the accuracy of the interpolated grid data based on point measurements at both monthly and daily time scales, geospatial factors (e.g., topography, latitude, longitude, distance from the sea, etc.) are used (Hofierka et al., 2002). Thus, the spatial and temporal factors are two controversial concerns for the grid-to-grid comparisons in the ground validation of the satellite precipitation and there is no a generalized model that satisfies the accuracy requirements for different locations and applications (Xu et al., 2015; Hiebl and Frei, 2018).

With growing interest into the long term and large scale, ranging from countrywide (Asong et al., 2017; Sharif et al., 2018; Sungmin and Kirstetter, 2018; Kumar et al., 2019; Gadelha et al., 2019) to worldwide studies (Sun et al., 2018), on the satellite precipitation evaluation, it is a challenge to find a decent compromise between, on the one hand, the representativeness of short-term variability, and, on the other hand, increasing the field of comparison (sampling area) relying on sparse measurement networks. It is also important to consider that the high density of the rain-gauge network may suffer from low maintenance introducing temporally variable errors in

the grids due to inconsistency of the measurements. Moreover, studies have shown that the variation of the station network over time can introduce temporal inconsistencies in grid datasets (Becker et al., 2013; Frei, 2014). Thus, using interpolation from a temporally invariant network of high quality could be more reliable to estimate the statistics of precipitation-geographic factor relationships that can later be applied in advanced interpolation procedures (Gottardi et al., 2012; Mergili and Kerschner, 2015) and gridding the point measurements. Due to the limitations discussed above about the application of grid-to-grid comparisons, many studies rely on point-to-grid evaluations (e.g., Sharifi et al., 2016; Xi and Liu, 2018; Hashemi et al., 2020). Regardless of the approach, the inherent difference between the point measurements and the areal satellite grids, i.e., a point of space in time accumulation versus a snapshot of time, has a major effect on the accuracy and precision of the evaluation results both quantitatively and qualitatively (Tang et al., 2018). Tang et al. (2018) presented a methodology for evaluating the efficiency of gauge density and introducing an optimum grid size for the comparison of ground-based and satellite-based datasets.

As mentioned earlier, the ground validation of GPM-IMERG products is in this dissertation was done in Paper I for over the entire Iran using grid-to-point comparisons.

2.1.4 Applications in hydrology

Due to the challenges of the satellite precipitation data evaluation directly using the gauged precipitation, an indirect evaluation can be done through comparing an estimated response, such as runoff, with the measured values (Wagner et al., 2012). Thus, if a satellite precipitation product results in a better runoff modelling, it is validated for this purpose. Therefore, utilizing the satellite precipitation data in regions with precipitation scarcity is possible if runoff measurements are available at the outlet of catchments. There were many studies that compared multisource satellite precipitation inputs for streamflow simulations (e.g., Mo et al., 2020; Musie et al., 2019; Zhang et al., 2019; Zhu et al., 2021).

Including the term "(streamflow OR runoff)" to the TI and AB parts of the search phrases in Table 1, the role of GPM and its precursor products in hydrological studies regarding runoff simulations, relative to other satellite precipitation products, can be specified better as in Table 2, which again shows the ratio of about one-third (=130/407). Note that the phrases can introduce some uncertainties and the results should be considered rough an estimation.

Table 2. Web of Science search results showing the importance and interest of GPM and TRMM and their corresponding algorithms IMERG and TMPA in the hydrology literature specified by runoff or streamflow.

Search phrase	Years	Number of results
(TI=(satellite AND (precipitation OR rain*) AND (streamflow OR runoff)) OR AB=(satellite AND (precipitation OR rain*) AND (runoff OR streamflow))) AND TS=(hydrolog*)	2018 – 2021	407
(TI=(satellite AND (precipitation OR rain*) AND **(GPM OR IMERG OR TRMM OR TMPA)** AND (streamflow OR runoff)) OR AB=(satellite AND (precipitation OR rain*) AND **(GPM OR IMERG OR TRMM OR TMPA)** AND (runoff OR streamflow))) AND TS=(hydrolog*)	2018 – 2021	130

2.2 Weather Radar (WR) Precipitation

2.2.1 Introduction and overview

Over the years it has been noticed that hydrologists face great issues in performing their work duties due to the inefficacy of proper hydrological data. Sometimes even if the data are available, their consistency is not satisfactory.

Of prominent importance, is the measurements of rainfall. The traditional rain gauge provides fairly accurate point measurements. However, there may also be a requirement for detailed measurements of the rainfall distribution over an extended area. The recent technological advancements have brought RS techniques, i.e., radar and satellite, to the field of hydrometeorology. It is likely that radar techniques will become the standard method of meeting these requirements at a catchment scale, because of the unique capability of radar to observe the areal distribution as well as temporal dynamics of precipitation. Also, this technology enables collection of the data from a centralized site. Thus, the maintenance is easier and the data from several regions (e.g., municipalities) can be immediately available for the users. A complete background review about this technology can be found in Harrold (1965), and Kessler (1966) regardless of the early-stage challenges faced at that time for the practical applications. A detailed report on the hydrometeorological application of radar data is documented in Browning (1978). Due to the immense technological progress, advancement in radar hardware, data processing, and data and signal analysis, the application of WR has become more common (Einfalt et al., 2004).

2.2.2 Types of WRs

The most common types of WRs worldwide include S-band, C-band, and X-band WRs. These radars scan the atmosphere in one or multiple elevation angles (levels) to generate a full azimuthal volume. The temporal resolution for each 360-degree scan depends on the rotational speed of the radar and the number of scanning elevations. Radars take the instantaneous reading of precipitation rate; so, the temporal resolution becomes very important for determining the actual rainfall

intensity. All the WRs usually obtain the reflectivity scans with certain time intervals. Temporal resolution, in general, roughly varies 10-15 min in the case of S-band, 5-10 min in the case of C-band and, 1-5 min in the case of X-WRs. The spatial resolution of these WRs also varies among 1000-4000 m for S-band, 200-2000 m for C-band, and 50-1000 m for X-band. The observational range could be limited to as large as 100-200 km for S-band, 100-150 km for C-band, and 30-70 km for X-band (Table 3). There are also other types of radar for only research purposes that are designed for high-resolution rainfall monitoring as high as 15 s in particular areas (Van de Beek et al., 2010; Mishra et al., 2016). Typical operating resolutions and maximum ranges for different types of WRs suggest that the X-WR gives higher temporal and spatial resolution compared to C- and S-band radars while covering shorter range (Table 3).

Table 3. Technical specifications for the typical X-, C-, and S-band WRs.

Parameters	X-band	C-band	S-band
Observation range (radius)	30 - 70 km	100 - 150 km	100 – 200 km
Temporal resolution	1 min	5 - 10 min	10 - 15 min
Spatial resolution	0.05 - 1 km	0.2 - 2 km	1 - 4 km
Antenna diameter	1 – 2 m	Up to 4 m	Up to 8 m
Wavelength	2.5 - 4 cm	4 - 8 cm	8 - 15 cm

Given the specifications above, X-WR seems to be appropriate for hydrological applications. According to a Web of Science search regarding the radar bands used in hydrology context, X-band and C-band WRs showed higher frequency than S-band during the past decade using the search phrases in Table 4. It should be noted that the total number of results without specifying the desired band was much higher (i.e., 1003) than individual band searches and the results should be considered as rough estimations of the importance.

Table 4. Web of Science search results showing the importance and interest of X-band WR in the hydrology literature over the past decade.

Search phrase	Years	Number of results
(TI=(radar AND (rain* OR precipitation)) OR AB=(radar AND (rain* OR precipitation))) AND TS=(hydrolog*)	2012 – 2021	1003
(TI=(**X-band** AND radar AND (rain* OR precipitation)) OR AB=(**X-band** AND radar AND (rain* OR precipitation))) AND TS=(hydrolog*)	2012 – 2021	58
(TI=(**C-band** AND radar AND (rain* OR precipitation)) OR AB=(**C-band** AND radar AND (rain* OR precipitation))) AND TS=(hydrolog*)	2012 – 2021	57
(TI=(**S-band** AND radar AND (rain* OR precipitation)) OR AB=(**S-band** AND radar AND (rain* OR precipitation))) AND TS=(hydrolog*)	2012 – 2021	24

The hardware specification and physics of the radar determine the spatial resolution of the rainfall data. Usually, X-WR has a shorter range and smaller antennas than C- and S-band radars therefore it typically functions with a finer radial resolution, and it can operate as low as 100-500 m spatial resolution. For this, recent studies suggest the use of observations at X-band frequency as an alternative or an addition

to S- and C-bands data (Lengfeld et al., 2013; Lengfeld et al., 2014; Trabal et al., 2013) to fulfil the requirements of urban drainage system modelling, rainfall–runoff models of rural river systems, hydraulic simulations, detailed information on extreme events, and many more. Besides higher resolution, radars operating at high frequencies benefit from lower costs resulting from smaller antenna size compared to long-wave radars. X-WRs can also derive reliable precipitation estimates close to the ground due to their relatively short range. S- or C-band radars measure within a range of hundreds of kilometres therefore, they cannot observe rainfall near the ground as the radar beam increases in height with increasing distance to the radar due to the elevation angle and the Earth's curvature. Also, measurements taken at a few kilometres in height above the Earth's surface need to be extrapolated to give an estimation of rainfall on the ground. These techniques are limited and imprecise, leading to large uncertainties in estimated reflectivity. In the last few years, the number of worldwide operational X-band WRs has rapidly been growing, thanks to an established technology that offers reliability, high performance, and reduced efforts and costs for installation and maintenance with respect to the more widespread C- and S-band systems, especially for small basins or urban areas (e.g., Antonini et al., 2014; Antonini et al., 2017; Shah et al. 2015; Chandrasekar et al. 2012; Van de Beek et al., 2010; Lengfeld et al., 2014). A report by the World Meteorological Organization (WMO) (Büyükbaş, 2009) states that the number of X-band WRs in use in WMO member countries has grown to almost 20% of the counted radars.

The C-band and S-band radars are more commonly used instruments for rainfall quantification as these radars do not suffer from signal attenuation as strongly as the X-WR (Van de Beek et al., 2010). This is because the X-WR has a shorter wavelength however, it can produce higher-resolution rainfall data with only a small antenna. This feature, in turn, makes the X-WR an affordable instrument for the spatial measurement of rainfall over distances as long as the signal attenuation is not a major problem (30-70 km radius). This characteristic has attracted the hydrometeorologists' attention, as early as 1980s, for better quantification of the rainfall and better water management due to the higher frequency and shorter wavelength of the X-WR.

In the 1980s and 1990s many universities and national institutes around the world employed mobile X-band Doppler radars to investigate the inner structures of rain and snow (Sharif and Ogden, 2014). For this, the X-WR is mounted in the back of the truck to chase the storms and quantify the local precipitation. However, recent studies suggest the X-WR as an alternative or addition to the C- and S-band radars to meet the urban drainage system modelling and urban flood warning system. Thus, the X-WR started to be installed in stationary condition on high ground and buildings for accurate real-time monitoring of rainfall events within the radar range, particularly, in the urban areas such as the X-WRs studied in this dissertation in

southern Sweden (Paper II and Paper IV) or those studied by VeVa collaborating initiated in the neighbouring country, Denmark (http://www.veva.dk/).

2.2.3 WR measurements and variables

The use of radar rainfall data has become very popular due to its accuracy and particularly due to its spatial and temporal resolution. WRs cannot measure precipitation directly; they measure reflectivity from particles along the radar's signal path. The polarimetric radar variables are reflectivity factor at horizontal polarization (ZH, or DBZH when presented in decibel by base 10 logarithm of the result of the division of ZH with the equivalent reflectivity of a 1 mm drop in a cubic meter volume), differential reflectivity (ZDR), differential propagation phase shift (PHIDP), specific differential phase (KDP), and the co-polar correlation coefficient (CC or ρhv). Using this information, the WR retrieval data are analysed to obtain the precipitation rate. Quantitative precipitation measurements with conventional X-, C-, or S-band WRs are conventionally based on the theoretical relationship between radar signal power, reflectivity, and rain intensity (Marshall and Palmer, 1948). The radar data are further processed to obtain the precipitation data and for that, the radar needs to be calibrated and validated accordingly.

2.2.4 Challenges and approaches

Validation and calibration of WR data are very important steps before the data can be utilized in hydrometeorological applications. The first step is to validate the rainfall data product obtained from retrieval data against the gauge measurement. As radar data is a type of remotely sensed data, one can expect discrepancies between the radar data and that of the rain gauges. For this, it is important that the radar data are well-calibrated and adjusted to obtain valid quantitative precipitation estimates. The common approach for calibration of X-WR data is to use the rain gauge data installed at different places in the catchment. The radar rainfall estimates are purely based on the empirical relationship between radar reflectivity and rain intensity that needs to be validated and calibrated using other types of ground measurements. These types of empirical calibration/validation have previously been documented by e.g., Jensen and Pedersen (2005), Rollenbeck and Bendix (2006), Pedersen et al. (2008; 2010), and Thorndahl and Rasmussen (2012).

Contrary to the long wavelengths of the C- and S-band radars, reflectivity measurement at the shorter wavelength, X-band, is largely attenuated by liquid water along the signal path. The rainfall signal attenuation at any distance depends on the drop size, distribution, and intensity of the rainfall/drops (Lengfeld et al., 2014). In severe cases, i.e., very high-intensity rain events, the X-WR is completely blocked, and no rainfall is recorded beyond the rain hotspot. This is seen as the major technical limitation of the X-WR in applications. To deal with this problem,

many scholars have suggested the implementation of a radar network. The network can consist of two or more X-WRs or a combination of C- or S-band with the X-WRs.

As illustrated in Figure 2, overshooting is another important source of error at large distances from the radar site, especially related to the higher-level scans.
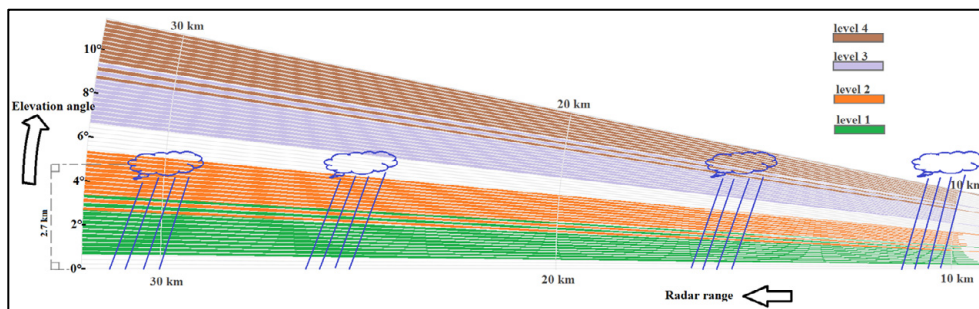
Figure 2. An example schematic illustrating how the rainfall from a cloud at an elevation of 3 km can be treated diversely with different levels (elevation angles) of the radar for different ranges.

WR data are typically produced and stored in polar coordinates that are cantered on the radar instrument, meaning that the radar sampling volume increases with the distance from the radar beam. Although, this type of dataset is applicable in weather forecast and meteorology, in other applications, i.e., hydrology, other coordinate systems are required. Furthermore, in many environmental applications, the WR data need to be integrated with geospatial data that are based on the Cartesian coordinate system (Sharif and Ogden, 2014).

In view of the above, the produced Polar coordinate data need to be converted to the Cartesian coordinate system. This, sometimes, requires high computational work, which may not be an issue considering contemporary computing technology. Data storage might be another practical limitation as the X-WR retrieves the rainfall return signal at up to six different levels around the radar and up to ~50-70 km radius every minute.

2.2.5 Radar hydrology and runoff applications

The impact of climate change on increased extreme rainfall events in many parts of the world calls for the development of a more efficient hydrological modelling. Based on the characteristics of urban hydrology and quick response time of runoff due to a higher percentage of impervious surfaces, higher temporal and spatial resolution rainfall data are an essential input to hydrological models to accurately simulate runoff and eventually proper design of the drainage system. Further, it is evident from previous studies that the uncertainty in urban hydrological models is

mainly due to errors in rainfall data (e.g., Willems, 2001; Thorndahl et al., 2008; Schellart et al., 2012).

Many researchers around the world have applied the high-resolution WR data to achieve accurate rainfall estimates for use in urban hydrology (e.g., Austin and Austin, 1974; Yuan et al., 1999; Han et al. 2000; Tilford et al., 2002; Smith et al., 2007; Krämer and Verworn, 2009; Villarini et al., 2010; Gires et al., 2012; Schellart et al., 2012; Schellart et al., 2014; Goormans and Willems, 2013). It is recommended that high-resolution spatial and temporal rainfall data, less than 100 m and 1 min, respectively, near the ground surface, are required for proper urban hydrological studies (Einfalt, 2003).

Although there has been a significant development in radar technology, i.e., hardware, signal processing, algorithms, etc., there are still differences between the rain gauge measurement and radar estimates. The quality for rainfall estimation relies on the methods and thorough knowledge of atmospheric physics and basic radar principles such as antennas, frequencies, bandwidths, polarization and processing the data for attenuation, removal of clutter, and conversion of reflectivity to rainfall. These fundamental facts and applications regarding WR have been described in detail in Bringi and Chandrasekar (2001), Meischner (2005), Doviak and Zrnic (2006), Michaelides (2008), Marshall and Palmer (1945), Austin and Austin (1974), Wilson and Brandes (1979), Smith and Krajewski (1991), Krajewski and Smith (2002), Einfalt et al. (2004), Delrieu et al. (2009), Krajewski et al. (2010), Villarini and Krajewski (2010), and Berne and Krajewski (2013).

In the following sections, the installed X-WR during the summer of 2018 in Dalby, southern Sweden is described and the radar processing algorithm and validation against a few rain gauges in the area is explained (mostly related to Paper II). Paper IV gives more examples of the single radar performance before calibration and after calibration with merging two X-WRs.

3 Study Areas and Data

3.1 Study areas

3.1.1 Iran (Paper I)

Iran is a mostly arid and semi-arid country located in Western Asia and is surrounded by Azerbaijan, Armenia, Caspian Sea, and Turkmenistan in the north, Oman Sea and Persian Gulf in the south, Turkey, Iraq, and Kuwait in the west, and Afghanistan and Pakistan in the East (Fig. 3).

Figure 3. A google map terrain view of Iran in western Asia.

Two high mountain ranges spreading from the northwest to northeast (Alborz) and from the northwest to central south (Zagros) generally limit the northern and western fronts to the central and eastern parts. Then, a majority of the central and eastern parts are deserts with low precipitation while maximum precipitations fall over north coasts with the Caspian see and western part of the country (Fig. 4).
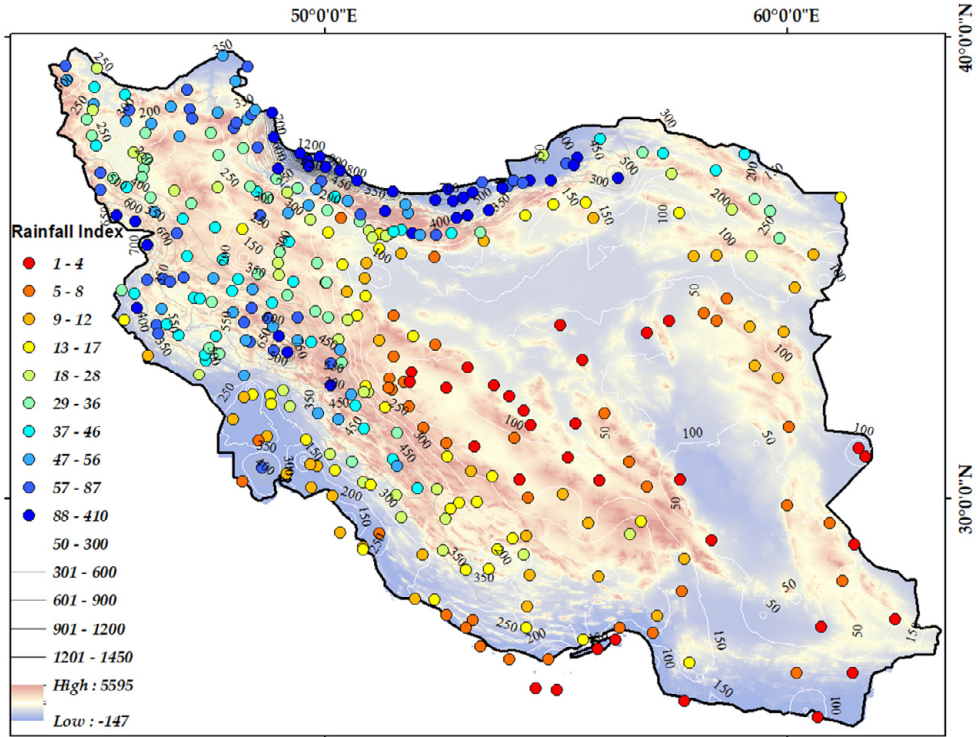
Figure 4. Background map of topography of Iran, labelled contourlines indicate mean annual precipitation by interpolating synoptic measurements at the stations denoted by colour-filled circles. Colour of circles shows rainfall index equal to the annual precipitation divided by average duration of dry spells using daily data (Paper I)

3.1.2 Karkheh River Basin (Papers III and V)

Karkheh River is among the three most hydrologically productive rivers of Iran that flows in west and southwest Iran until it ends at the Hawizeh Marshes or Hoor-al-Azim on Iran-Iraq border (Fig. 5). Majority of the river basin area that is located in Zagros mountains, upstream area of the Karkheh Dam, is studied in Papers III and V. The study area is divided into five sub-areas (labelled by letters A to E in Figs. 5) that comprise the following sub-catchment areas: Gamasiab (A: 11,500 km^2), Qarasu (B: 5,500 km^2), Seymareh (A, B, and C: 29,400 km^2), Kashkan (D: 9,500 km^2), and, KRB, the entire catchment area of Karkheh Dam, which is located at the outlet of the basin (A, B, C, D, and E: 42,900 km^2).
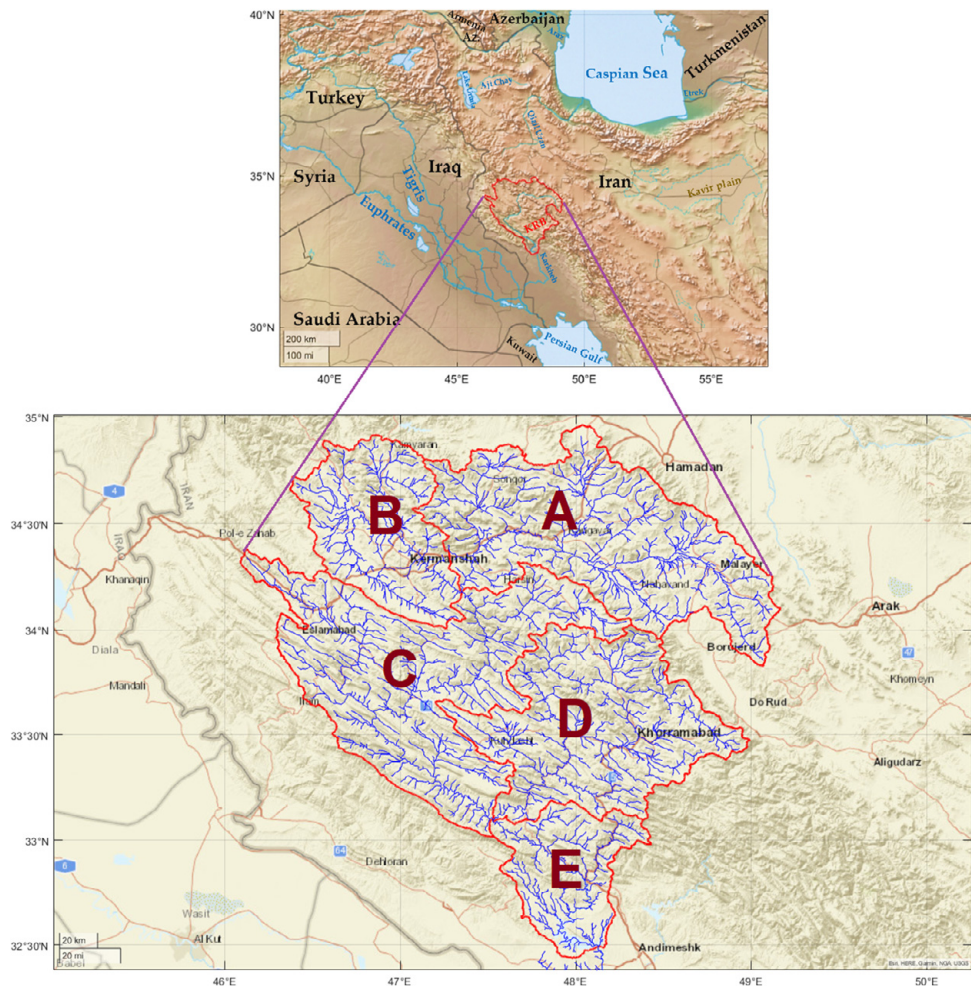
Figure 5. The location of Karkheh River in west and southwest Iran including the sub-catchment areas in Zagros Mountains: Gamasiab (A), Qarasu (B), Seymareh (A, B, and C), Kashkan (D), and KRB, the entire catchment area of Karkheh Dam, (A, B, C, D, and E).

Being in operation since 2002, Karkheh reservoir, at the outlet of KRB, is the largest artificial lake in the country and has experienced reduction of inflow that could affect hydropower generation, food production, and vulnerable wetlands downstream. Increased upstream water withdrawals due to increased population and agricultural development, as well as impacts of global warming are considered important factors. However, lack of knowledge about the share of each factor could exacerbate the condition due to additional uncertainties in the undertaken management strategies. Therefore, Paper V, used a Budyko approach, supported by

hydrological modelling (using HBV), to separate impacts of climate variation and human activities on runoff for the sub-catchments of KRB.

3.1.3 X-band WRs in south Sweden (Paper II and IV)

The X-WRs in Sweden were installed for in Dalby and Helsingborg Cities, southern Sweden, in 2019 and 2020, for operational use by VA Syd and NSVA, respectively (Fig. 6). Prior to that, a pilot test installed the same device in Dalby. The technical specifications of the X-WRs are listed in Table 5 according to the manufacturer.
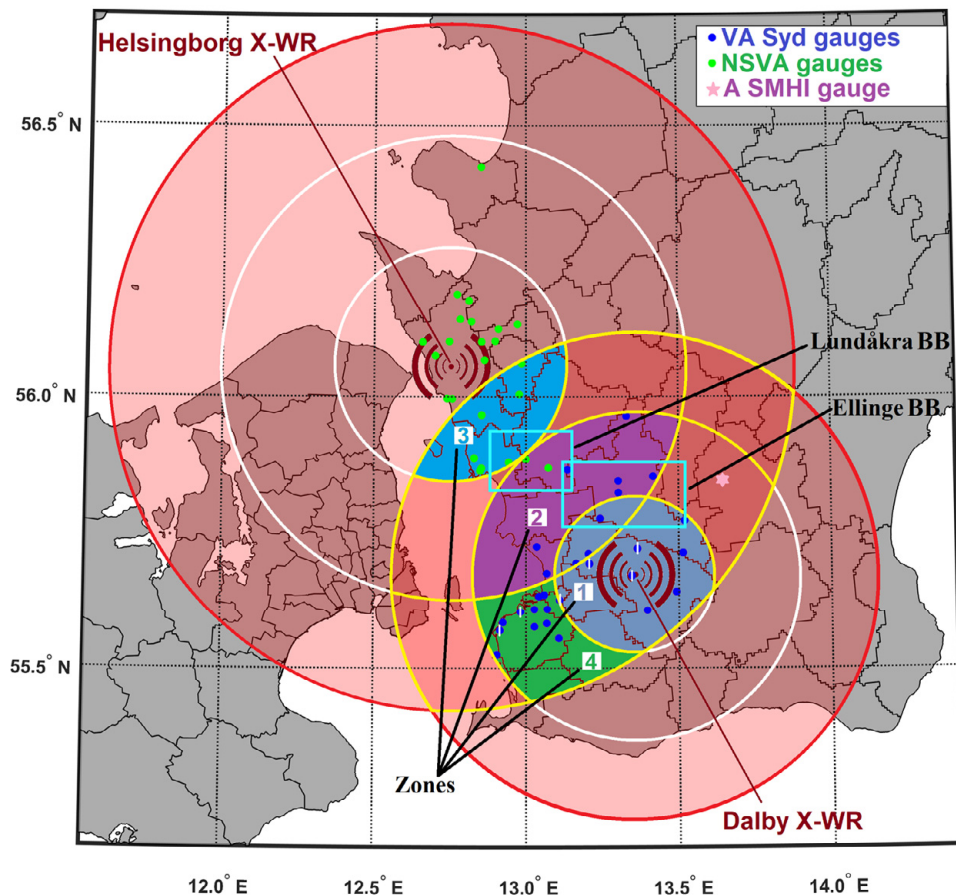
Figure 6. The two X-band WRs in southern Sweden covering multiple tipping bucket rain gauges in the overlapping coverage and beyond by VA Syd and NSVA. The coloured polygons labelled 1-4 are four zones that encompassed all the 38 tipping buckets (and an example SMHI gauge at Hörby) in the overlapping area. The boundaries of the polygons were defined based on three rings around each X-WR corresponding to the one-third, two-thirds and full range radiuses. The two blue regtangles are bounding boxes for two sub-catchment areas of the Lundåkra and Ellinge treatment plants.

Table 5. Specifications of the Compact Dual Polarimetric X-band Doppler Weather Radar WR-2100 (FURUNO).

Parameters	Descriptions
Antenna Polarity	Dual polarimetric (Vertical and Horizontal), Simultaneous transmission/receiving
Operating Frequency	9.4 GHz band
Beam Width	2.7 degrees (both horizontal and vertical beams)
Peak Output Power	100 W (both horizontal and vertical beams)
Vertical Scan Angle	-2 to 182 degrees (adjustable)
Antenna Rotation Speed	16 rpm max. (adjustable)
Observation Range	60 km max.
Scan Modes	PPI, Volume Scan, Sector PPI, Sector RHI
Output Parameters	Reflectivity factor Zh (dBZ), Doppler velocity V (m/s), Doppler velocity width W (m/s), Cross polarization difference phase φdp (deg), Specific differential phase KDP (deg/km), Correlation coefficient between two polarizations ρHV, Differential reflectivity factor ZDR, Rainfall intensity R (mm/h) (see Appendix 1)
Data Correction	Distance attenuation, Rain attenuation, Doppler Velocity Folding
Doppler Speed	+/-48 m/s
Unwanted Signal Removal	Land and vessel clutter suppression and Interference Rejection
Operating Temperature	-10 to +50 °C
Maximum Wind Survival Speed	60 m/s
Power Supply	100-240 VAC, Single Phase, 50/60 Hz

Paper II studied the single X-WR in Dalby during the pilot test (3-July-2018 14:14 UTC to 12-Sep-2018 12:21 UTC), while Paper IV studied the overlapping coverage area of the two X-WRs in Dalby and Helsingborg for May-September 2021. Therefore, Figure 6 shows the coverage of the two X-WRs with some additional information such as the location of tipping bucket rain gauges operated by the water utility companies of VA Syd and NSVA (coloured points). Those gauges used for the pilot test (Paper II) of a single X-WR in Dalby are indicated with a white vertical line crossing the blue points. These and all the other gauges within the overlapping area were used in Paper IV for evaluating both the single and merged X-WR rainfall estimations. Merging data from two X-WRs (Paper IV) was needed because of inconsistent rainfall estimation with single radar and single levels depending on the range and elevation angle of the sampling location of radar.

3.2 Study Data

3.2.1   Synoptic weather stations data (Paper I)

All synoptic stations shown in Figure 4 with available daily precipitation data across Iran were studied as ground truth for the GPM-IMERG products (Paper I) during the study period April 2014 to December 2017. In total, 403 stations were under operation across the country during the study period, of which 368 and 349 had at least two and three years of daily records, respectively.

3.2.2 GPM-IMERG products (Papers I and III)

The GPM-IMERG precipitation data used for ground validation (Paper I) included three daily products (IMERG-Early, -Late, and -Final) and a monthly product (IMERG-Monthly). The spatial resolution of all the IMERG products were $0.1° \times 0.1°$ (about 11 km on the equator). The ground validation analyses were made at daily, monthly, and annual time scales by comparing the observations of each station with the corresponding grid encompassing the station.

The two near real-time runs of the IMERG algorithm give IMERG-Early and IMERG-Late products originally in half-hourly time scale with about 4 hours (shorter for the second halves of hours) and 14 hours (shorter for recent data) latency, respectively. IMERG-Late uses data from more satellites than IMERG-Early and, can employ a two-way (forward and backward) morphing process as it includes two overpasses of the satellites. The IMERG-Final is a bias-corrected product relying on monthly observations from the global rain gauge network GPCC (Global Precipitation Climatology Centre). Therefore, it is available with a minimum latency of 3.5 months and cannot be useful for near-real time applications. NASA comments that IMERG-Late and IMERG-Final products are similar (mainly over oceans, and, to a lesser extent, over land).

For the satellite-based monthly runoff modelling in KRB (Paper III), data from the IMERG-Late product were used for all grids whose centres were within the boundary of the sub-catchments Gamasiab, Qarasu, Seymareh, Kashkan, and KRB as defined in Figure 5. It should be noted that the available IMERG product data for Paper III were from June 2000 (Version 6) while the data for Paper I were from the previous version (when IMERG was only run for the GPM era from 2014).

3.2.3 MODIS Terra data and products (Paper III)

As part of the satellite data-driven modelling of monthly runoff in KRB (Paper III), a few MODIS Terra satellite-based input variables were used (along with IMERG-Late) to consider the effects such as evapotranspiration, vegetation index and soil moisture. MODIS stands for the Moderate Resolution Imaging Spectroradiometer, and Terra is one of the two satellites for MODIS program that together observe the entire Earth every 1–2 days in 36 wavelength bands with different resolutions (250, 500, and 1000 m for different bands). The composite (combination of other data sources and Terra data) and band data from MODIS that were used for monthly runoff modelling in KRB are as summarized in Table 6.

It is noted that the length of record, spatial resolution and revisit time are important aspects of RS data to be used in hydrological modelling. Despite the higher resolution and temporal coverage of Landsat, in comparison to MODIS, (30–100 vs. 250–1000 m), it has a longer revisit time (16 days vs. daily). Also, geostationary satellites with rather continuous temporal resolution usually operate at too coarse

spatial resolution. Sentinel 2A and 2B, that together present a more balanced spatiotemporal resolution (5–10 days and 10–60 m) has limited length of records (since 2015 and 2017, respectively).

Table 6. MODIS Terra product or band data used for monthly runoff modelling in KRB (Paper III).

MODIS Terra product	Variables	Resolution
MOD16A2v006 (Running et al., 2019) composite product data	Evapotranspiration actual (ET) and potential (PET)	8-day and 500-m
MOD13A3v006 (Didan et al., 2015) product and band data	* Normalized Difference Vegetation Index (NDVI) and band 7 (B7)	Monthly and 1-km

* studies used B7 (Chu, 2018) and NDVI (Wang et al., 2007) as predictor variables for soil moisture estimation.

3.2.4 Runoff data (Paper III and V)

Monthly average flow data at the outlet of the five Karkheh sub-catchments (as defined in Fig. 5) were studied as reference for calibration and verification of satellite data driven monthly runoff modelling (Paper III). Daily runoff data were used in Paper V as input to the HBV runoff modelling for the same sub-catchments. Figure 7 illustrates a statistical overview of the runoff values during the common period between September 1999 to September 2017 (corresponding to 18 complete water years in Iran)
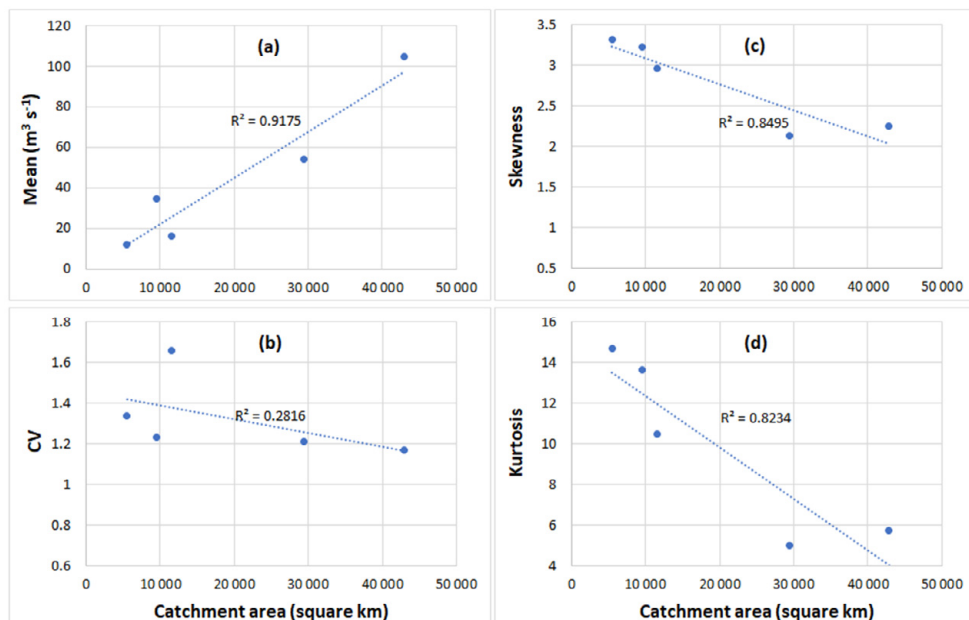
Figure 7. Variation of mean (a), coefficient of variation (b), skewness (c), and kurtosis (d) of the average monthly runoff by catchment size for the five sub-catchment areas of KRB during September 1999-September 2017.

The average of mean monthly runoff at the outlet of Gamasiab, Qarasu, Seymareh, Kashkan, and KRB was about 16.3, 11.8, 54.2, 34.4, 104.3 $m^3 s^{-1}$, respectively (Fig. 7a). As shown in Figure 7a, the mean runoff increases by catchment size. However, the coefficient of variation (standard error normalized by mean runoff), skewness (asymmetry compared to normal distribution), and kurtosis (degree of presence of outliers in the distribution) decrease by catchment size (Figs. 7b-d).

3.2.5   Tipping buckets data (Papers II and IV)

The tipping bucket data were used as reference for rainfall data validation estimated by the X-WRs. The distribution of these gauges in the study areas is shown in Figure 6. It is noted that the number of tipping buckets in the overlapping coverage area of the two X-WRs was 38 (29 by VA Syd and 9 by NSVA) in 2021 and lower in the past. The location information is listed in Table 7.

Table 7. Latitude and lingitude of the tipping bucket rain gauges located in the overlapping coverage of the X-WRs in Dalby and Helsingborg at their max range of 50 and 70 km, respectively (the first 29 gauges are for VA Syd and the remaining ones for NSVA).

No.	Stations	Latit.	Longit.	No.	Stations	Latit.	Longit.
1	Arlöv PST*	55.636	13.059	20	Turbinen PST*	55.605	12.982
2	Arlöv NYA	55.627	13.110	21	Limhamn PST	55.585	12.924
3	Eslöv VV	55.846	13.302	22	Augustenborg	55.577	13.027
4	Marieholm PST	55.867	13.136	23	Bulltofta VV	55.610	13.069
5	Billinge VV	55.964	13.330	24	Hammars Park PST*	55.570	12.915
6	Kungshult VV	55.854	13.417	25	Höja TS	55.583	13.068
7	Löberöd PST	55.773	13.519	26	Klagshamn ARV	55.525	12.904
8	Örtofta PST	55.777	13.243	27	Sjölunda ARV	55.633	13.042
9	Harlösa ARV	55.714	13.514	28	Oxie PST	55.555	13.107
10	Ellinge ARV	55.824	13.303	29	Rosendal PST	55.609	13.027
11	Lomma Hamn	55.676	13.068	30	Asmundtorp	12.943	55.880
12	Bjärred TS	55.725	13.035	31	Billeberga	13.000	55.885
13	Norra Verket TS	55.712	13.204	32	Billesholm	12.986	56.061
14	Dalby Godemansvägen*	55.672	13.347	33	Ekeby	12.978	56.004
15	Genarp PST	55.608	13.397	34	Landskrona	12.853	55.869
16	Södra Sandby PST*	55.721	13.365	35	Landskrona p14	12.829	55.888
17	Veberöd TS	55.642	13.492	36	Lundåkra	12.849	55.865
18	Lund Råbyvägen*	55.694	13.208	37	Teckomatorp	13.073	55.870
19	Källby ARV	55.694	13.164	38	Vallåkra	12.854	55.966

* The gauges used in the pilot test (Paper II).

Every record of the rain gauge, tipping bucket type, had a resolution equal to 0.2 mm rain-depth. Therefore, the temporal resolution of the gauge observations could vary by rainfall intensity. For a consistent use of tipping buckets as reference for radar estimations (originally at minute scale), event-based cumulative rainfall hyetographs (in Paper II) and 5-min aggregations (in Paper IV) were used.

It is worth mentioning that the study period for Papers II, and IV was in summer 2018, and summer 2021, respectively. Hence, the rainfall terminology was preferred over precipitation in the X-WR context of this dissertation.

4 Methodology

4.1 Ground validation of satellite precipitation (Paper I)

4.1.1 Statistical analyses

The ground validation of the GPM-IMERG satellite precipitation products was performed by comparing all the available gauge-satellite data pairs. Satellite data from GPM-IMERG were available in grids of $0.1° \times 0.1°$ size. The equivalent ground truth data were collected from the synoptic gauges across Iran as shown in Figure 4. The statistical criteria were defined as listed below:

$$\text{- Mean absolute error: MAE} = \frac{\sum_{i=1}^{n}|S_i - O_i|}{N} \tag{1}$$

$$\text{- Correlation coefficient: CC} = \frac{\sum_{i=1}^{n}(S_i - \bar{S})(O_i - \bar{O})}{\sqrt{\sum_{i=1}^{n}(S_i - \bar{S})\sum_{i=1}^{n}(O_i - \bar{O})}} \tag{2}$$

$$\text{- Relative bias: rBIAS} = \frac{\sum_{i=1}^{n}(S_i - O_i)}{\sum_{i=1}^{n}O_i} \ or \ \frac{\bar{S} - \bar{O}}{\bar{O}} \tag{3}$$

$$\text{- Probability of detection: POD} = \frac{n_{11}}{n_{11} + n_{10}} \times 100 \tag{4}$$

$$\text{- False alarm ratio: FAR} = \frac{n_{01}}{n_{11} + n_{01}} \times 100 \tag{5}$$

$$\text{- Percentage frequency of overestimations: Over} = 100 \times \frac{N1}{N} \tag{6}$$

$$\text{- Percentage frequency of underestimations: Under} = 100 \times \frac{N2}{N} \tag{7}$$

$$\text{- Percentage frequency of close estimations: Equal} = 100 \times \frac{N - N1 - N2}{N} \tag{8}$$

where S_i and O_i are satellite estimation and gauge observation at time i, respectively. n_{11}, n_{01}, and n_{10} denote the number of times that satellite and gauge both detected rain, satellite did not confirm the gauge record, and gauge did not confirm the satellite record, respectively. N is total number of the compared satellite-gauge data pairs. $N1$ is the number of times that $S_i - O_i$ is bigger than 0.25 mm d^{-1} or $0.1 \times O_i$ while $N2$ is the number of times that $O_i - S_i$ is bigger than 0.25 mm d^{-1} or $0.1 \times O_i$.

There are several statistical criteria used for the ground validation of satellite precipitation (Wang et al., 2017). Some of them such as mean absolute error (MAE) and relative bias (rBIAS) measure the error between the two datasets and some others, such as the probability of detection (POD) and false alarm ratio (FAR), evaluate the detecting abilities of the satellite sensors. By focusing on the dependency of these criteria on the nature of rainfall and considering that what (point) is being compared to what (grid), these statistics might not show the actual reliability of the satellite datasets in a region or compared to other locations with completely different nature of rainfall. For example, MAE is the average magnitude of the individual errors, so lower values of it are generally favourable. However, it can result in a misleading interpretation. For example, in a dry location with a percentage of zero values higher than 90%, where intense rainfalls are then rare, MAE will not reflect it if there are a few huge individual errors related to the extreme weather which are important to estimate. On the other hand, rBIAS calculates the accumulated individual errors (overall bias) relative to the accumulated observed rainfall during the period of comparison, so it can show both the overall under/overestimations (according to the negative or positive sign) and a comparable bias value for different locations. Anyway, the use of MAE together with rBIAS is essential. While a low magnitude of both MAE and rBIAS implies stronger evidence of a good performance of the satellite product, a combination of a large magnitude of rBIAS with a low MAE for a site may be due to a -usually- low magnitude of individual errors a long with a few huge errors. This situation is more likely to appear for dryer sites with a higher frequency of minor rainfalls. Also, a low magnitude of rBIAS should not be ignored if a large MAE exists. Furthermore, a low magnitude of rBIAS means that the total amount of rainfall observed in a site is closely estimated by the satellite product during the period of comparison, in another word, the sum of the positive individual errors is almost equal to the sum of the absolute values of the negative individual errors, regardless of the magnitude of the individual errors or correlation between the two datasets.

4.1.2   Geospatial and temporal analyses

To assess whether the performance of IMERG products could be related to the geospatial, climatic factors, or time of the year, the indices introduced above were separately calculated for some regional categories based on elevation, slope, latitude, longitude, and rainfall index (i.e., average annual rainfall/mean dry period) as well as temporal categories such as months and seasons. The calculated indices for each category can then be illustrated by box plots. Such analyses help to discern dependencies of the satellite precipitation performance to different factors, which is useful for the selection of input variables for bias corrections.

4.2 Evaluation of radar rainfall (Papers II and IV)

Theoretically, the radial resolution (range resolution) is a function of radar pulse length, therefore, could be very small. In practice, however, it is governed by the storage and data transmission limitations (Thorndahl et al. 2017). The range resolution for the radar in Dalby was set at the fixed intervals of 50 meters during the pilot and operational use. Table 8 presents the bin area and the equivalent rectangle width in different ranges of the radar. As an example, the equivalent rectangle for a bin area in the range of 1 km is 50×47 m^2 (0.24×10^{-2} km^2) while it increases to 50×471 m^2 (2.4×10^{-2} km^2) in the range of 10 km for 2.7º beam width. The average heights of the sample boxes as a function of distance from the radar location (range) are presented in Table 8. For example, while the sampling volume in the 6 km range of the radar in the first scanning level is almost 200 meter above the ground, for the ranges as much as 40 km the sample volume from the fourth elevation scan has around 7 km height (Table 8).

Table 8. Estimated radar bins, the equivalent rectangle width, and sampling height in different ranges of Dalby XR.

Range (km)	Radar bin area (×10⁻² km² or hectare)	Equivalent rectangle width (m)	Sampling box height above the horizon for different elevation scans (m)			
			L1 (2°)	L2 (4°)	L3 (8°)	L4 (10°)
0.05	0.01	2.4	1.7	3.5	7.0	8.8
0.5	0.12	24	17	35	70	88
1	0.24	47	35	70	141	176
5	1.2	236	175	350	703	882
6	1.4	283	210	420	843	1058
10	2.4	471	349	699	1405	1763
19	4.5	895	663	1329	2670	3350
20	4.7	942	698	1399	2811	3527
30	7.1	1414	1048	2098	4216	5290
40	9.4	1885	1397	2797	5622	7053
50	11.8	2356	1746	3496	7027	8816

The X-WRs in southern Sweden give a rainfall estimation using a built-in procedure to the X-WRs. The underlying equations for these single level rainfall estimations, which are named RATE by the manufacturer involve three dual polarization variables, namely, DBZH, ZDR, and KDP (these variables were introduced earlier in section 2.2.3), using the equations described in Paper II. Radar rainfall equations are usually based on the Marshall-Palmer relationship, representing an exponential relationship between the radar reflectivity measurements and rainfall intensity. RATE product of the X-WRs used the same relationship with a corrected horizontal reflectivity (DBZH) based on ZDR and KDP (Paper II).

### 4.2.1 Evaluating RATE using tipping buckets (Papers II and IV)

The dual polarization observations and RATE calculations for the X-WRs were at the azimuthal sweeps of less than 0.5° and the radial resolution of less than 100 m at a revisit (overpass) time interval of about one minute at each elevation angle scans. To evaluate the high-resolution precipitation estimations by such radars, local tipping bucket rain gauges (as shown in Fig. 6) data were used in two ways:

- Visual investigations using cumulative and non-cumulative hyetographs (Paper II: using the Dalby X-WR)

- Statistical analyses of 5-min aggregated data using some goodness-fit-criteria as well as quantile-quantile plot (Paper IV: using the both X-WRs)

The equivalent radar data for a gauge location could be based on the closest radar bin (the projection of each radar sampling volume on the cartesian plane).

Hyetographs

The hyetographs showed rainfall depth data distribution (in cumulative or non-cumulative form) over time using bar charts for gauges and lines for RATE data at every 1-min timestep. In the cumulative form, for example, a hyetograph could look like as in Figure 8. An interpolated rainfall estimation that is also presented in this figure will be described in the following section.
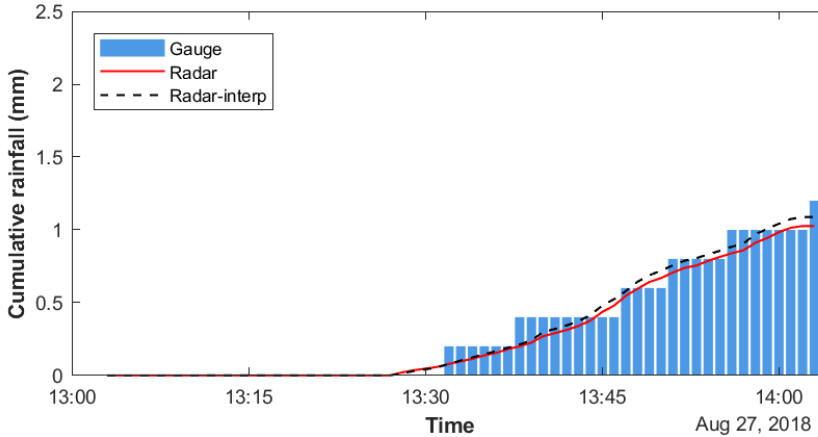
Figure 8. Cumulative hyetograph during the first 30-min period of a rainfall event observed in Arlöv gauge station in summer 2018. In this example, radar shows RATE data from the closest bin of the Dalby X-WR at elevation angle 10°. Radar-interp, stands for the interpolated (weighted average) rainfall from the adjacent bins that intersected the closest bin.

4.2.2 Projection to cartesian

Figure 9 shows how bins of a radar are distributed over the ground in comparison to the square grids due to the polar observations.
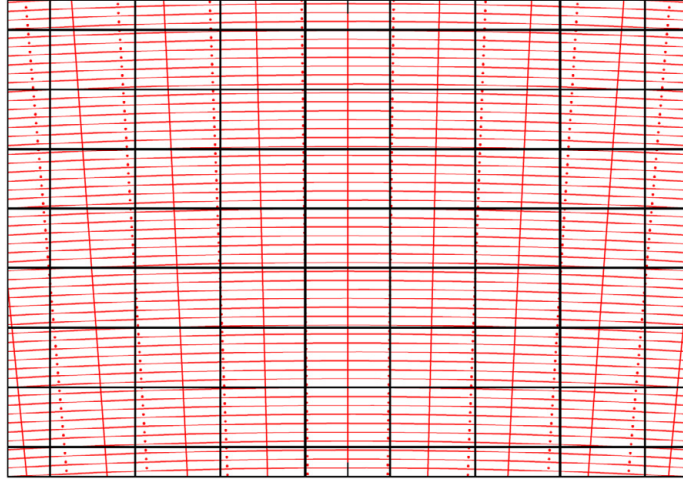
Figure 9. Typical intersections of the 150m × 1º polar radar bins (red) with the 1000 m × 1000 m square grids (black) (Sharif and Ogden, 2014).

According to the specifications of the X-WRs presented in Table 5, the beam angle was 2.7°. Therefore, the average azimuthal change for every sweep (<0.5°) was a few times smaller than the beam width. Thus, there are overlaps for adjacent bins from a few neighbouring scan-lines. Figure 10 shows an example of three consecutive sweeps (scanline) illustrated in three different colours (red, grey, and green in a clockwise azimuthal direction, respectively). Accordingly, an exemplary radar bin of size 50 m × 2.7º from Dalby X-WR, which is located between 4.95 km and 5.00 km ranges and azimuthal angles of 358.2º–0.9º (marked in bold black in Fig. 10), can be divided into three areas a_1, a_2, and a_3. While the radar only reports the rainfall obtained from the grey scanline for this bin, the information from other scanlines (red and green) can be disregarded. From the simple arithmetic relationships (inspired by Sharif and Ogden, 2014), the radar output can be adjusted by considering the information from all the scanlines with an overlap area within a given bin. For the bin highlighted in Figure 10, this can be presented as:

$$R - intrp = \frac{R_r(a_1+a_2)+ R(a_1+a_2+a_3)+ R_g(a_2+a_3)}{2(a_1+a_3)+3a_2} \qquad (9)$$

where R is the RATE reported for the bin by X-WR while *R-interp* is the amount obtained after considering R_r and R_g, the other RATEs from two adjacent scanlines (red and green, respectively) with overlaps within the initial scanline.
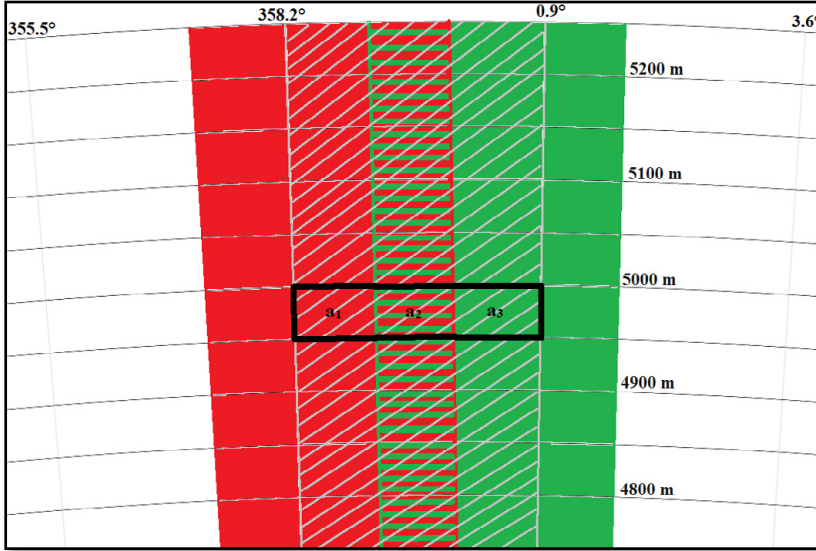
Figure 10. Schematic of three consecutive sweeps (scanlines) of the radar in a few ranges around 5 km, in red, grey and green in a clockwise azimuthal direction, respectively.

Thus, the programmed code is capable of interpolating the retrieval data for the existing radar bins by giving a weight to each neighbouring bin based on its overlapping area within the target bin. It is estimated that depending on the spatial complexity of the local rainstorm, there are differences between the interpolated and raw data of radar.

In many applications of WRs, such as for weather warning systems, remapping to regular grids is inevitable for integrating meteorological information from different sources such as networks of X-, S-, and C-band radars, satellites, and weather stations, which are typically sampled in different coordinate systems. Also, providing inputs to the hydrological models requires rainfall amounts presented in regular grids (Sharif and Ogden, 2014).

4.3 Satellite data driven runoff modelling by ANN

In remote mountainous catchments where weather stations are lacking, it is not possible to locally validate the accuracy of RS data. So, the calibration of

conceptually based runoff models that usually require accurate inputs can be challenging. The computationally advanced data driven models such as artificial neural networks (ANNs) that are skilful in non-linear function fitting may indirectly consider the bias correction of satellite inputs when modelling runoff. However, in large catchments, the wealth of input variables from many satellite grids may not be easily useful without physical equations. As a result, more collective input variable would be generally preferred. Although the use of average precipitation over catchment could be a basic input, Paper III introduced a few new collective input variables based on the areal coverage ratio of satellite precipitation over the catchment. Accordingly, to have more than one input variable of this type, coverage ratios for a few categories of total precipitation depth were formulated. These variables were named event- and catchment-specific areal precipitation coverage ratios (ECOVs and CCOVs, respectively). The categories used for CCOVs were based on 11 constant denominators while the categories used for ECOVs were variable from one event (i.e., a month) to another as they were calculating the ratio of the catchment area that received higher than 50, 75, 100, 125, 150, and 200% of the appeared average areal precipitation in the event.

4.3.1 Artificial Neural Networks

ANN modelling which are sometimes called deep learning modelling is among well-known AI methods introduced for the non-linear function fitting problems in hydrology. Structurally, an ANN is a combination of neurons spread over a few hidden layers in between an input layer and an output layer, as shown in Figure 11, coloured in red, black, and blue. Once the input variables introduced to a model of specified architecture, a random scalar weight (w) and bias (b) is applied to each input variable by the corresponding neurons on the input layer (black nodes in Fig. 11) in form of multiplication and addition, respectively ($n = w \times x_i + b$, where x_i is a vector of data for an input variable). Then, a non-linear activation function can project the resulted value, usually, over (-1,1) as is the case for the hyperbolic tangent sigmoid function in Figure 12. The projected values will then comprise inputs to the neurons on the next layers, and so on. Once all weights and biases were initialized, the model can calculate a vector of estimations for the output variable y (y'). Then, ANN considers the mean squared errors for the estimations (MSE) as a loss function of weights and biases that should be solved for minimization in several iterations based on a gradient descent or Jacobean algorithm (as described in Hagan et al., 1997). MATLAB comments that the so-called backpropagation Levenberg-Marquardt algorithm is usually the fastest method for training moderate-sized feedforward neural networks (up to several hundred weights).
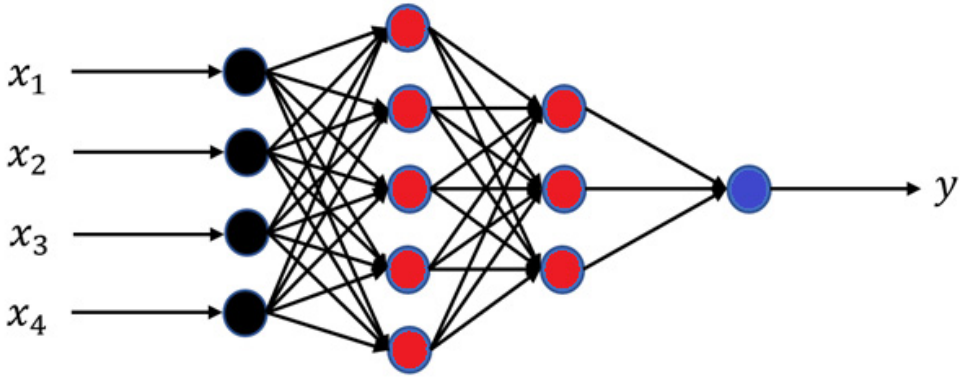
Figure 11. Architecture of a feedforward ANN with two hidden layers (including red neurons) and four input variables $x_1,\ldots,x_4$ to estimate output variable y.
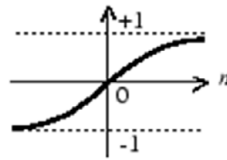
Figure 12. The shape of a hyperbolic tangent sigmoid function applied to the neuron values n.

4.3.2 Overfitting and generalization

There are several ways to analyse and prevent the overfitting issue for the ANNs. A basic way is obtained by dividing the available dataset for calibration into two portions, namely, training and validation. Then, the training dataset is the only data directly used for parameterization of the ANN while MSE is also calculated for the validation set at each iteration. The validation is a popular in-process way to address overfitting problems that threaten any ANN modelling based on the use of many parameters (weights and biases). Accordingly, a continuous increase in MSE for the validation dataset, while MSE is decreasing for the training dataset, by iteration is considered an overfitting signature. In Paper III, a maximum validation fail was introduced to stop modelling if the increase of MSE for validation for six consecutive iterations. Paper III (and, as it will be shown later, Paper IV) further analysed the performance of the ANNs using another portion of data that was neither used in training nor in validation. This portion is called testing or verification.

An adjusted k-fold cross validation/verification process was used to divide the dataset into 5 folds where each fold received random, but equal number of, data from each of the twenty categories of runoff including 0-5, 5-10, 10-15, …, 95-100 percentiles. Then, calibration-validation-verification were possible in 20 ways for selecting a fold for testing, a fold for validation, and rest for training, k×(k-1).

Moreover, the generalization was pursued further by combining outputs of several ANNs after repeating the parameterization with different random initialization of weights and biases under a specific assumption for the modelling to do not stuck in local minimums and avoid noisy estimates. The possible assumptions were based on the choice of calibration-validation-verification fold, input variable combination, and ANN architecture. While the initial parameterization repeated only 10 times per modelling assumption, since the architecture choices alone let 420 repeats (one or two hidden layers with 1-20 neurons per layer, 20×21), for a given fold and input variable 4200 repeats were tried out. In paper III, an arithmetic average of six top-ranked models based on six statistical criteria (during calibration) was reported for each fold choice for testing (i.e., k=5). Thus, finally, five hybrid models (with different testing folds) per input variable combination were reported and analysed. A complete list of input variable combinations is listed in Table 9 (Paper III).

Table 9. Combinations (Comb.) of input variables (P: precipitation, ET: actual evapotranspiration, PET: potential evapotranspiration, NDVI: Vegetation index NDVI, B7: MODIS Band 7, SM: seasonal runoff, P_p: perturbations of P from the seasonal P, CCOVs: coverage ratios for 10 catchment-specific categories, and ECOVs: coverage ratios for 6 event-specific categories). Refer to Paper III for more information.

Comb.	class	Input variables	Comb.	class	Input variables
1	A	P, P_p, PET, SM	7	B	P, P_p, ECOVs, PET, NDVI, SM
2	A	P, P_p, CCOVs, PET, SM	8	B	P, P_p, CCOVs, ECOVs, PET, NDVI, SM
3	A	P, P_p, ECOVs, PET, SM	9	C	P, P_p, ET, PET, NDVI, B7, SM
4	A	P, P_p, CCOVs, ECOVs, PET, SM	10	C	P, P_p, CCOVs, ET, PET, NDVI, B7, SM
5	B	P, P_p, PET, NDVI, SM	11	C	P, P_p, ECOVs, ET, PET, NDVI, B7, SM
6	B	P, P_p, CCOVs, PET, NDVI, SM	12	C	P, P_p, CCOVs, ECOVs, ET, PET, NDVI, B7, SM

4.3.3 ANN performance score by statistical criteria

As summarized below, a set of statistical criteria were used to compare the runoff estimations ($\hat{y}_i$) to the corresponding observed values (y_i).

- Pearson correlation coefficient: $PCC = \dfrac{\sum_{i=1}^{N}\left((y_i-\mu)\times(\hat{y}_i-\hat{\mu})\right)}{\sqrt{\sum_{i=1}^{N}(y_i-\mu)}\times\sqrt{\sum_{i=1}^{N}(\hat{y}_i-\hat{\mu})}}$ (10)

- Nash-Sutcliffe efficiency: $NSE = 1 - \dfrac{\sum_{i=1}^{N}(y_i-\hat{y}_i)^2}{\sum_{i=1}^{N}(y_i-\mu)^2}$ (11)

- King-Gupta efficiency: $\text{KGE} = 1 - \sqrt{(PCC-1)^2 + \left(\dfrac{\hat{\sigma}}{\sigma}-1\right)^2 + \left(\dfrac{\hat{\mu}}{\mu}-1\right)^2}$ (12)

- Root mean square error: $\text{RMSE} = \sqrt{\dfrac{\sum_{i=1}^{N}(y_i-\hat{y}_i)^2}{N}}$ (13)

- Relative absolute error: $\text{RAE} = \dfrac{\sum_{i=1}^{N}|y_i-\hat{y}_i|}{\sum_{i=1}^{N}|y_i-\mu|}$ (14)

- Mean absolute error: $\text{MAE} = \frac{\sum_{i=1}^{N}|y_i - \hat{y}_i|}{N}$ (15)

where, i is the index of time ($i = 1, 2, \ldots, N$ in months), μ and σ are mean and standard deviation of runoff observations y_i in MCM (million cubic meters); $\hat{\mu}$ and $\hat{\sigma}$ are mean and standard deviation of runoff estimates $\hat{y}_i$ in MCM. More information about these statical criteria can be found in Paper III.

4.4 Merging QPE by two X-WRs

As discussed in Paper IV, and mentioned earlier, due to inconsistent rainfall estimation by single-device X-WR operation, depending on the radar range and level (from Paper II), merging X-WR data based on the range and level was evaluated in this dissertation.

As shown before in Figure 6, the four zones in the overlapping area of the Dalby and Helsingborg X-WRs could be used to develop a merged X-WR QPE. Accordingly, two methods (linear regression and ANN) were used to develop a separate model for each zone.

RMP refers to the regression-based hybrid of Marshall–Palmer type estimations of rainfall. With the RMP model, the six single-level RATE products (RATEs) built into the X-WRs were combined based on a linear regression model without intercept (Paper IV). However, the input variables to the ANNs did not include RATEs. Instead, the ANN inputs were 5-min dual X-WR variables (here, RHOHV, KDP, VRAD, DBZH, and ZDR from the six vertical levels; five from Dalby and one by Helsingborg X-WR) for the equivalent bins for the 38 ground-truth gauges. The data period relied on the available radar data and the utilized data was based on the gauge-detected events whose MGI>2 mm h^{-1} (maximum gauge intensity). This threshold selected an event if at least one out of the 38 gauges recorded more than 1 mm rainfall in a half an hour time step of the event to focus on moderate to extreme events. Accordingly, the number of input-output data pairs were:

- 16,500 from 11 gauges for Zone I
- 14,200 from 9 gauges for Zone II
- 9,200 from 7 gauges for Zone III
- 14,500 from 11 gauges for Zone IV

Due to the high number of data, the chance for overfitting based on a shallow network could be smaller than the case for satellite-based runoff modelling described before. However, the generalization would be still interesting to avoid local minimums and find the best outcome. Thus, 6000 random parameterization repeats per zone were used that allowed for random choice among multiple ANN settings such as ANN architecture (two hidden layers by 5-30 neurons on each), and

dataset partitioning ratios (50, 55, and 60% for training and 20 or 25% for testing, remaining for validation) in each repeat. The maximum validation fail was raised to 10. In the end, a repeat with the best validation result was considered to fix the parameterization. For comparability, the RMP models were developed based on the same calibration data (training and validation) as in the finally selected ANN.

For the rainfall, rather than runoff, a majority of the 5-min observations was comprised of zero or small values. Therefore, rather than the adjusted k-fold process introduced for runoff, the focus for the division of rainfall data variability to calibration-validation-testing was on higher percentiles. Thus, equivalent portion of training-validation-testing were selected from each of the following categories: <95%, 95–97.5%, 97.5–99%, 99–99.9%, and > 99.9%.

Finally, the selected model based on ANN and RMP were analysed for testing portion of the data using the following verification scores (Paper IV):

- Relative bias: $\text{rBIAS} = 100 \times \frac{\sum (E_t - O_t)}{\sum O_t}$ (16)

- Mean absolute error: $\text{MAE} = \frac{\sum |E_t - O_t|}{N}$ (17)

- Pearson CC: $\text{PCC} = \frac{\sum ((O_i - \bar{O}) \times (E_t - \bar{E}))}{N \times \sigma_o \times \sigma_e}$ (18)

- Nash-Sutcliffe efficiency: $NSE = 2 \times \frac{\sigma_e}{\sigma_o} \times \text{PCC} - \left(\frac{\sigma_e}{\sigma_o}\right)^2 - \left(\frac{\mu_e - \mu_o}{\sigma_o}\right)^2$ (19)

- King-Gupta efficiency: $\text{KGE} = 1 - \sqrt{(\text{PCC} - 1)^2 + \left(\frac{\sigma_e}{\sigma_o} - 1\right)^2 + \left(\frac{\mu_e}{\mu_o} - 1\right)^2}$ (20)

- Probability of detection: $\text{POD} = 100 \times \frac{H}{H+M}$ (21)

- False alarm ratio: $\text{FAR} = 100 \times \frac{F}{F+H}$ (22)

- Gilbert skill score: $\text{GSS} = 100 \times \frac{H - Hr}{H + F + M - Hr}$ (23)

where, E and O denote estimated and observed rainfall, respectively, $Hr = (H + F) \times (H + M)/(H + F + M + R)$, and H, M, F, and R are frequency values related to four possible rainfall detection conditions: hits (correct alarms), misses, false alarms, and correct rejects. Considering the 0.2 mm resolution of the ground-truth observations by tipping buckets, H, M, F, and R were defined as below.

- H: the number of time steps where $O_t \geq 0.2$ and $E_t > 0$

- M: the number of time steps where $O_t \geq 0.2$ but $E_t = 0$

- F: the number of time steps where $O_t = 0$ but $E_t \geq 0.2$

- R: the number of time steps where $O_t = 0$ and $E_t < 0.2$

5 Results and Discussions

5.1 Satellite Precipitation Validation

The comprehensive evaluation of the GPM-IMERG products over Iran can be found in Paper I. Here, I discuss some example results with more explanations considering the descriptions presented in section 4.1.1 about the evaluation of the criteria values. Figure 13 shows quantile-quantile plots for five arbitrary sites from Paper I. These locations showed different combinations of correlation coefficient (CC), MAE, and rBIAS values. Looking carefully at these plots, it can be discerned that at sites no. (1) and no. (2) deviations from the 45-degree line are less compared to the other sites, so the satellite product for these two sites performed a bit better than site no. (3) and much better than site no. (4) and no. (5) in resembling actual daily data distribution. This is while the correlation values for the sites no. (1) and no. (2) are significantly different. Moreover, the performance of the satellite product for sites no. (3) and no. (5) are completely different, while they both showed a high correlation (0.79) and a similar MAE (~0.7 mm/day). Therefore, rBIAS could play a more discriminating role than a misleading CC. On the other hand, we know that data from any point in a satellite grid (e.g., rain gauge) is not an excellent representative of that grid, so the errors that were attributed to the satellite products using rBIAS are not necessarily actual errors. Instead, it can also be an indication of spatiotemporal variability of rainfall for that location within a grid. This could be more discussed using the detection criteria such as FAR. As seen in the boxplots presented in Figure 14 (from Paper I), the general increase of FAR for the dryer bins (lower rainfall index) suggests that very local rainfall events are more probable to appear in dryer locations. In such conditions, a rainfall event affects partially a grid while it is not observed by a gauge located in a dry part of the grid. Conversely, the chance for this condition is reduced for the wetter locations (higher rainfall index), which sounds to be reasonable.
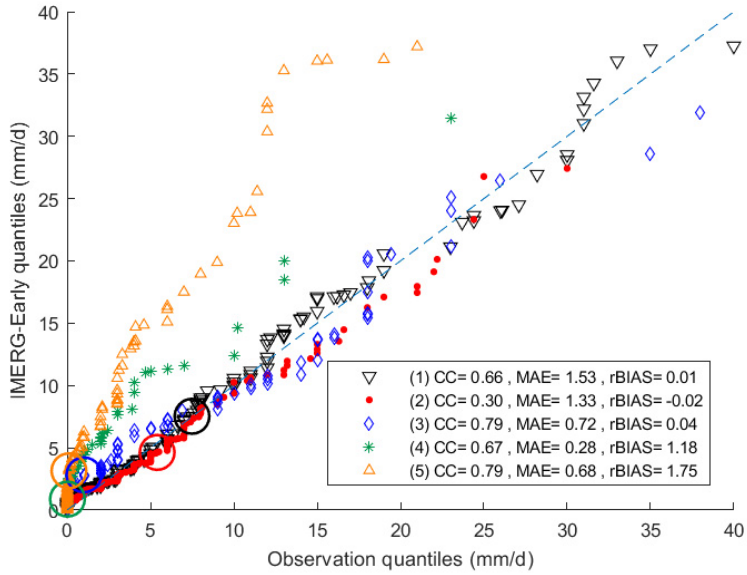
Figure 13. Q-Q plots for comparing different combinations of CC, rBIAS, and MAE in five sites where very small values of rBIAS are showing better performances of the IMERG-Early in estimating observed precipitation quantiles for different combinations of CC and rBIAS (The large circles' center shows the position of the 95 percentile).
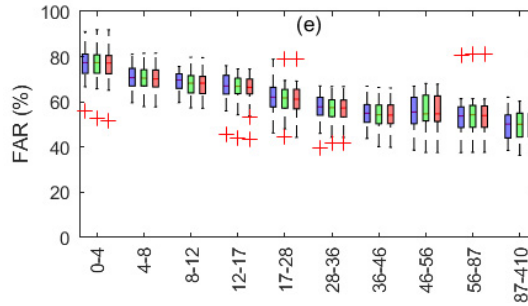
Figure 14. Box plots of the criteria indices for the ten rainfall index bins (horizontal axis), in blue, green, and red corresponding to the IMERG-Early, IMERG-Late, and IMERG-Final products, respectively. The horizontal line in the middle of boxes, and the upper and lower bounds of the boxes are the 50th, 75th, and 25th percentiles, respectively. The red plus symbols denote the outlier data and the whiskers (dashed black lines), extend to the most extreme data not considered outliers. There are equally around 40 stations used for each bin.

In contrary to the observed variation of satellite precipitation performance for different classes of rainfall index (such as a decreasing trend in Fig. 14), the trends were not that interesting to interpret with high confidence based on the other geospatial factors. Some examples are given in Figure 15 and 16.
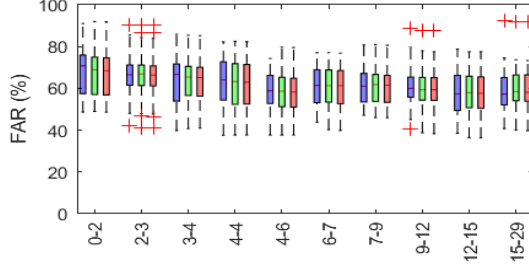
Figure 15. FAR boxplots for 10 classes of slope in blue, green, and red corresponding to the IMERG-Early, IMERG-Late, and IMERG-Final products, respectively.
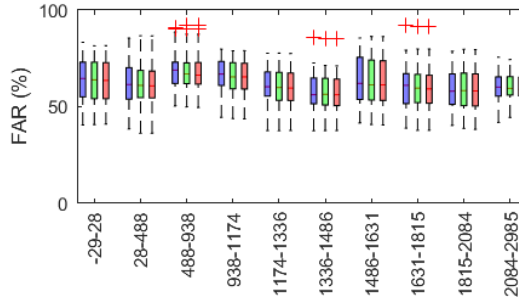
Figure 16. FAR boxplots for 10 classes of elevation in blue, green, and red corresponding to the IMERG-Early, IMERG-Late, and IMERG-Final products, respectively.

5.2 Evaluating X-WRs (Papers II and IV)

5.2.1 Single X-WR QPE for pilot test (Paper II)

As described before, a method of this dissertation for the evaluation of X-WR QPE was based on hyetographs that can be found in Paper II. Additional analyses are presented here by evaluating local variability of rainfall based on the interpolation method introduced in section 4.2.2. Figure 17 shows the rainfall variability in an event observed at three different bins. These bins were in the ranges of 1, 19, and 30 km of the Dalby X-WR encompassing the location of the tipping bucket gauges in Dalby, Arlöv, and Hammars Park. As a result, the differences between the rainfall estimations from the single-bin and interpolated multiple bins (overlapping the single-bin) were possible at every rate. More visible differences are at local peak values where the interpolated rainfall (Radar-interp) is lower than the single-bin estimation. Accordingly, we decided to use single-bin data for QPE in Paper IV to better represent local gauge measurements (more in the next section).
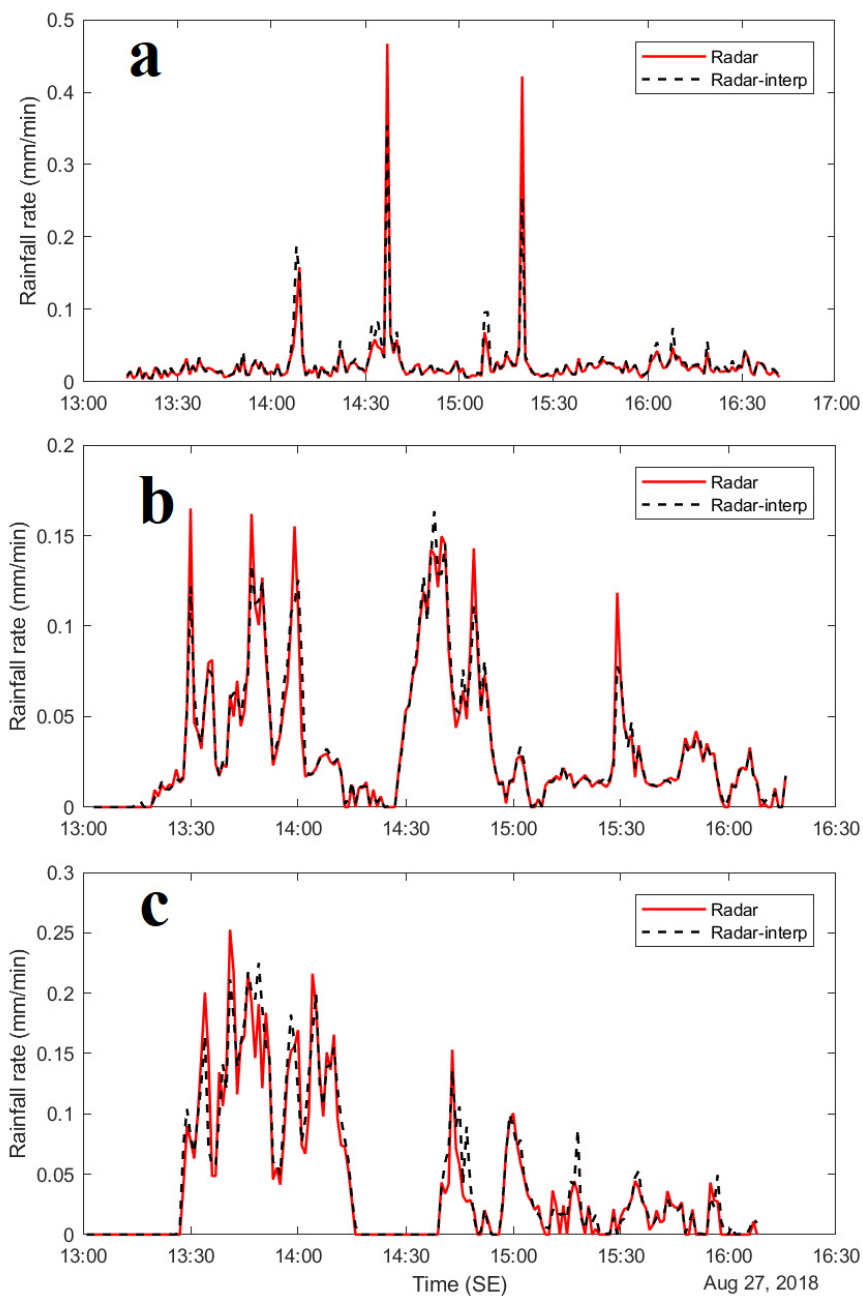
Figure 17. Difference between rainfall intensity from single-bin and interpolated multiple bins for a rainfall event observed at three radar bins at 1 (a), 19 (b), 30 (c)-km ranges and elevation angle of 2°.

Looking at the examples for a specific bin (at Arlöv station) but at different elevation angles as in Figure 18, some moments of the event are generally missed at the higher elevation angles. Also, the estimated rainfall at higher level (Fig. 18.a) is generally smaller in magnitude. Since the distance and direction from the Dalby X-WR were the same for the two plots in Figure 18, we cannot attribute the difference between them to the attenuation. Instead, as shown in Table 8, the higher altitude of the sampling volume for L4 compared to L1 may be a result of overshooting of part of the storms. For hyetographs comparing the radar-gauge data refer to Paper II.
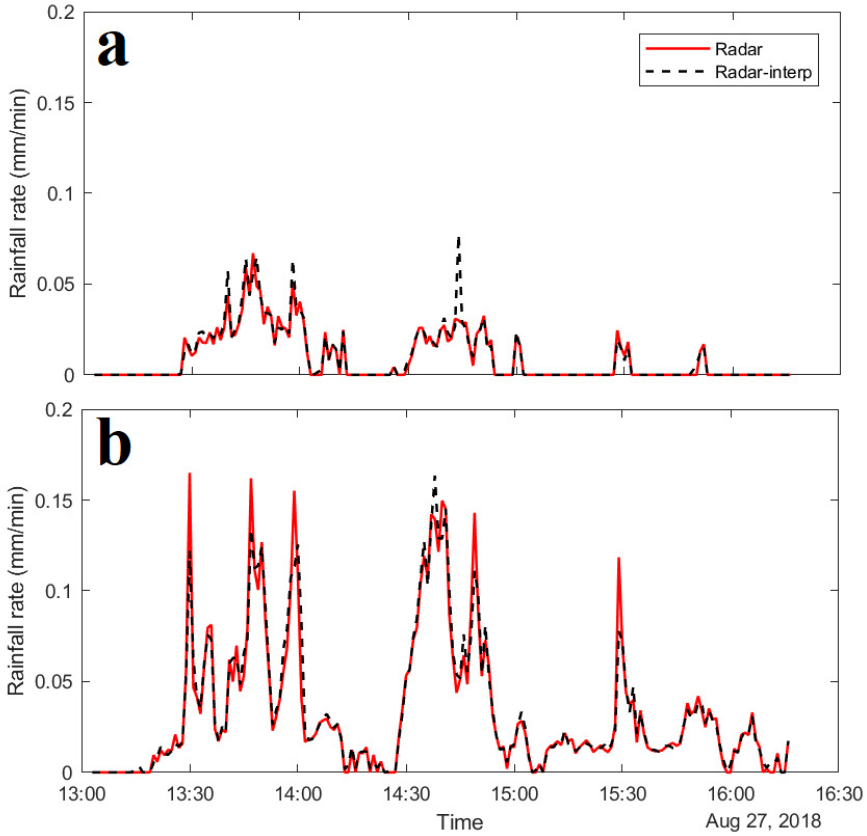
Figure 18. Level 4 (a) vs. Level 1 (b) rainfall estimation for an event observed by the Dalby X-WR at Arlöv station.

5.2.2 Single vs. Merged X-WR QPE (Paper IV)

Figure 19 summarizes four of the studied statistical criteria evaluating the performance of the single level products (RATEs: R_H, R_{D1}, R_{D2}, …, R_{D5}) and merging models (RMP and ANN) for different zones. Generally, improved verification scores from RATEs to RMP and ANN are observed for all zones by the

61

decrease of rBIAS (Fig. 19a) and MAE (Fig. 19d) and increase of GSS (Fig. 19b) and NSE (Fig. 19c) from left to right. A problematic single level was related to R_{D1} that belonged to the elevation angle 1.5° of Dalby X-WR, susceptible to ground clutter and contaminated radar measurements especially for Zone IV (in the direction towards Malmö City). Except that, Zone III (the farthest to Dalby X-WR and closest to Helsingborg X-WR) generally was the most problematic region according to GSS and MAE.
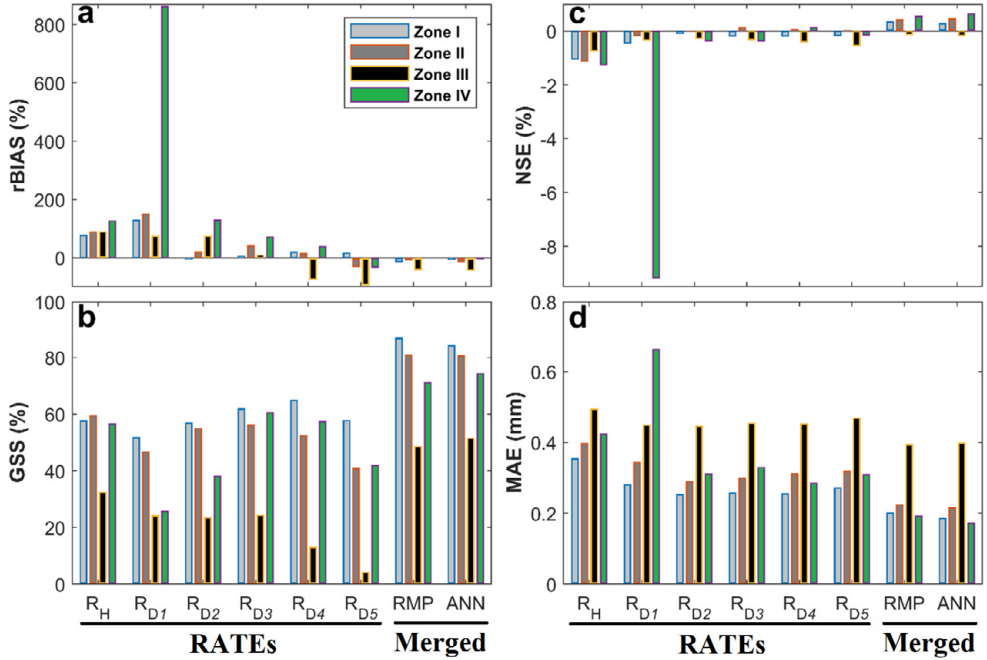
Figure 19. The verification scores rBIAS (a), GSS (b), NSE (c), and MAE (c) for the single level products (RATEs: R_H, R_{D1}, R_{D2}, …, R_{D5}) and merging models (RMP and ANN) for different zones based on the data portions that were not used in the calibration of ANN and RMP (testing).

5.2.3 Gridded radar data for urban runoff modelling

To evaluate the produced data by X-band WRs outside of the gauges' locations, all rainfall estimations within two catchments named Ellinge and Lundåkra were studied (within the bounding boxes shown in Fig. 6 and as shown in Fig. 20 and 21). Accordingly, 5-min radar rainfall estimations in the bins were rescaled to grids of 500-m size for the catchment areas using the mass-conserving method as described in Sharif and Ogden (2014). The only assumption added here was that the bins are rectangular although they have slight curvature in the azimuthal direction. The examples given in Figures 20 and 21 show the distribution of local tipping buckets in or around the Ellinge and Lundåkra catchments, respectively.
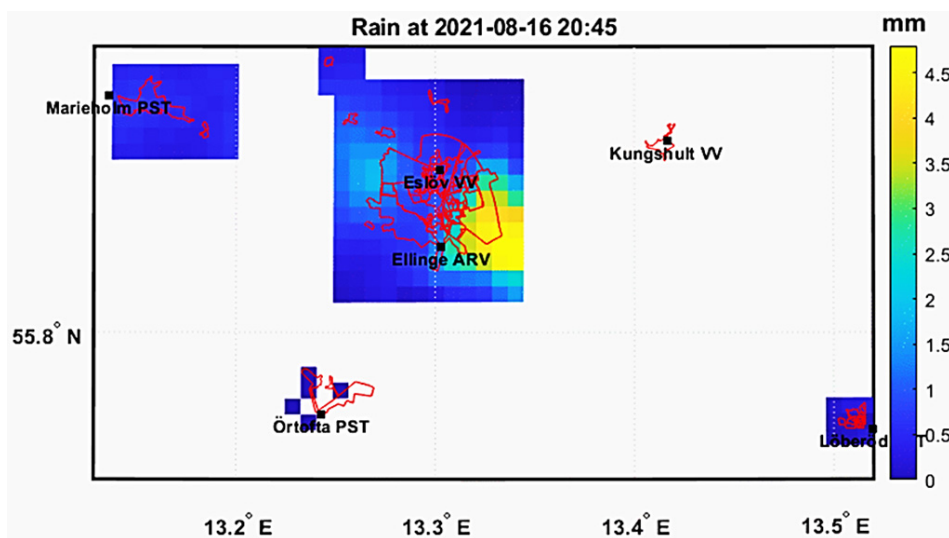
Figure 20. An example illustration of a gridded rainfall product for the Ellinge catchment. The map shows the rainfall depth at a 5-min time step of an event on August 16, 2021 between 20:45 and 20:49:59.
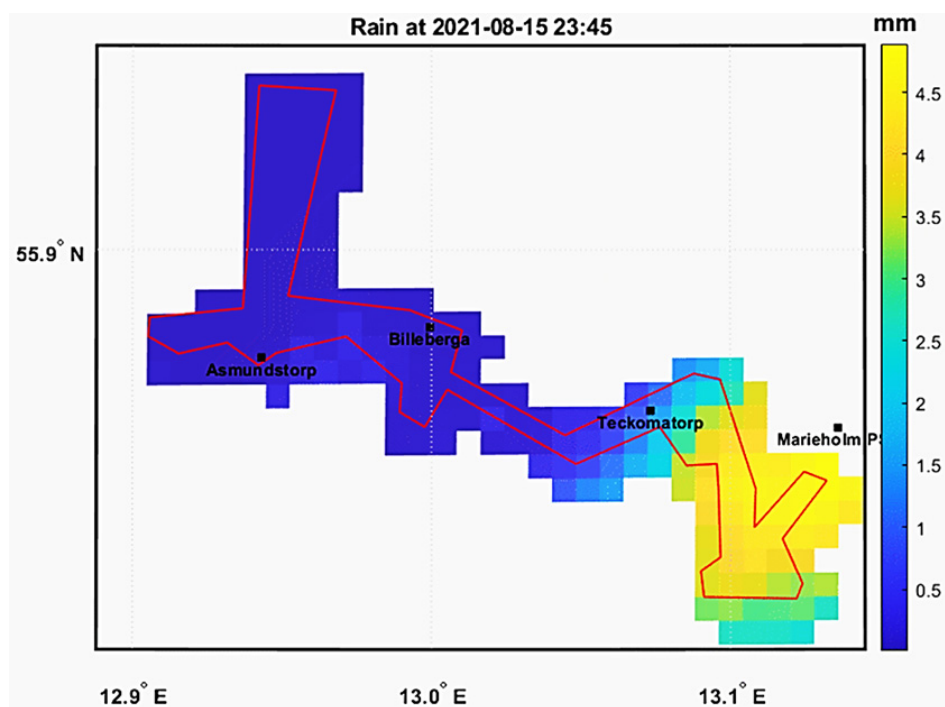
Figure 21. An example illustration of a rainfall product for the Lundåkra catchment. The map shows the rainfall depth at a 5-min time step of an event on August 15, 2021 between 23:45 and 23:49:59.

The underlying mering model or RATE used for the catchments are summarized in Table 10. The reason for not using Zone III models for runoff modelling was that it revealed the most erroneous rainfall estimations for the merging models. Although some parts of Lundåkra were in Zone III, they were not too far from Zone II where we observed much better rainfall estimates based on X-WRs.

Table 10 The underlying zone RATE and merging model used in different grids for the studied catchments.

Catchment	RATE	Merging model
Ellinge	R_{D2} (all the grids)	ANN model of Zone I (for the grids in Zone I) ANN model of Zone II (for the grids outside of Zone I).
Lundåkra	R_H (all the grids)	ANN model of Zone II (for all the grids).

The catchment rainfall products were then saved in the multi time-step GIS ASCII files and sent to the water utility companies, NSVA and VA Syd, for rainfall-runoff modelling. They used a pre-calibrated model based on MIKE Urban+ and re-ran it for a few additional inputs such as local gauges and C-band WR, along with the X-WR products described earlier (Table 10) as part of a research collaboration project. Also, it is noted that the X-WR data that were based on separate events were gap-filled by the data from the local tipping buckets for running the rainfall-runoff model. Based on the returned runoff results from VA Syd and NSVA, further analyses were made using MAE, CC, and NSE (as in eq. 17-19, but using the observed vs. modelled runoff data). The resulted scores were calculated for the selected event periods during May-September 2021 as summarized in Table 11 and Table 12 for the Ellinge and Lundåkra catchments, respectively. In Table 11, The highest NSE and CC and lowest MAE were obtained for ANN. According to the results, the merged product helped to improve runoff modelling in the Ellinge catchment as compared to the other available inputs. In Table 12, the values of the three criteria under ANN as input were rather comparable to those under local rain gauges as input for Lundåkra, so these inputs obviously outperformed the other two inputs (i.e., R_H and C-band WR). The negative NSE for some inputs such as C-band WR at both catchments shows a worse performance than using average runoff as an estimator, according to the definitions given earlier about NSE. It is noted that the catchment runoff values were based on the pump stations in the sewage system rather than direct measurement of flow. Therefore, a degree of uncertainty in the modelling could be related to the unwanted time lags between rainfall and runoff measurements. The studied sub-catchments were rather small (as can be seen from Figs. 6, 20, and 21) where tipping buckets existed rather densely. Therefore, it can be argued that in catchments with lower density of local gauges, more benefits of X-WRs to the runoff modelling could be observed.

Table 11. Statistical performance criteria for the runoff modelling in Ellinge using different input variables at 5-min time scale (available observed and modelled runoff data pairs from the selected events, May-September 2021, for the runoff modelling were used in the evaluations).

Rainfall input	MAE (l/s)	CC	NSE
Local tipping buckets	20.11	0.62	0.15
SMHI station at Hörby*	43.58	0.05	-0.92
ANN (X-WR merged)	15.75	0.77	0.54
C-band WR	44.09	-0.03	-0.34

* see the location in Figure 6.

Table 12. Statistical performance criteria for the runoff modelling in Lundåkra using different input variables at 5-min time scale (available observed and modelled runoff data pairs from the selected events, May-September 2021, for the runoff modelling were used in the evaluations).

Regnindata	MAE (l/s)	CC	NSE
Local tipping buckets	4.83	0.76	0.19
R_H (X-WR RATE)	5.53	0.82	-0.13
ANN (X-WR merged)	5.14	0.75	0.10
C-band WR	6.52	0.53	-0.27

5.3 Satellite-based monthly runoff modelling (Paper III)

For the monthly runoff simulation using ANN, the k-fold process described in section 4.3.2. left 41, 41, and 123 pairs of input-output datasets for testing, validation, and training, respectively. For a certain combination of input variables (Table 9) and maximum lag time (0, 1, or 2 months), five hybrid models (each an arithmetic average of the six top-ranked models in calibration based on the criteria in equation 10-15), corresponding to the number of fold choices for testing, were obtained. As a result, a set of figures each comprising four plots, equivalent to four combinations of the input variables within each class (Table 9) for each lag time was produced. The selected model per plot had the lowest test RMSE. Thus, Figures 22-26, equivalent to the KRB sub-catchments, illustrate the selected figures that included the best model for the sub-catchments. For example, for Gamasiab (Fig. 22), based on the performance criteria for testing (values coloured in red), Comb. 7 and Lags 2 resulted in the highest PCC, NSE, and KGE (0.95, 0.90, and 0.93, respectively) and the lowest MAE, RAE, and RMSE (16.12 MCM/month, 0.30, and 27.76 MCM/month, respectively) compared to other competing models.

Moreover, the mean ± standard deviation (M±SD) of the performance criteria for the five hybrid models per plot was calculated for all data partitions (values coloured in blue in Fig. 22-26). Lower SD at optimal M (i.e., minimum MAE, RAE, and RMSE or maximum PCC, NSE, and KGE) implies more robust runoff modelling regardless of data partitioning. From the M±SD values in Figure 22, modelling under Comb. 8 and Comb. 7 had comparable results, while both outperformed

modelling under Comb. 5. For instance, the M value for KGE in Comb. 5 is 0.87 while it is 0.93 and 0.91 under Comb. 7 and Comb. 8, respectively (Fig. 22). Similar outperformance was observed for testing alone, where, e.g., RMSE and RAE were reduced by over 7 MCM/month and 19%, respectively, under Comb. 7 in relation to Comb. 5. The lower SD under Comb. 7 and Comb. 8 (e.g., ±0.03 for KGE) compared to Comb. 5 (e.g., ±0.07 for KGE) implied robust modelling for Gamasiab when ECOVs alone (Comb. 7) or together with the CCOVs (Comb. 8), were combined with the catchment-scale input variables (i.e., P, PET, NDVI, and SMs). For all catchments (Fig. 22-26), an input combination from class B or C (Table 9) with a max lag of 1 or 2 months resulted in the best modelling according to:

- For Gamasiab (Fig. 22), Comb. 7 and Lags. 2

- For Qarasu (Fig. 23), Comb. 12 and Lags. 1

- For Seymareh (Fig. 24), Comb. 7 and Lags. 2

- For Kashkan (Fig. 25), Comb. 7 and Lags. 1

- For KRB (Fig. 26), Comb. 12 and Lags. 2

It can be inferred that the memory of the hydrologic system, concerning the influence of the previous state of input variables, is longer for Gamasiab, Seymareh, and KRB (catchment sizes > 11,000 km^2) than for Qarasu and Kashkan (catchment sizes < 10,000 km^2), perhaps due to the higher storage capacity. However, the best combination of input variables was Comb. 12 for both the smallest (Qarasu) and the largest (KRB) catchment, while Comb. 7 was best for other sub-catchments. Referring to Table 9, Comb. 12 from class C incorporates B7 and ET as additional variables compared to Comb. 7 from class B which incorporates ECOVs in addition to the catchment-scale basic variables in classes A and B. However, the ECOVs for Qarasu appear to be more useful than in KRB since the second-best model for Qarasu was obtained under Comb. 11 while this was Comb. 9 for KRB.

In general, the difference in the best combination of input variables for different sub-catchments can be interpreted in two ways: inadequacy of the coverage ratios, or necessity to include more variables such as soil moisture. Among the catchments, Kashkan and Gamasiab had the weakest and strongest modelling performance, respectively, based on RAE, CC, NSE, and KGE. RAE was 0.5 and 0.3, CC was 0.86 and 0.95, NSE was 0.73 and 0.90, and KGE was 0.77 and 0.93 in the testing of the selected models for Kashkan (Fig. 25) and Gamasiab (Fig. 22), respectively. As discussed in Paper III, these two catchments had the highest and lowest variation of the catchment-scale monthly precipitation, respectively. Therefore, the weaker performance may be related to the insufficient calibration limited by the length of the satellite data. Also, higher ±SD of the performance criteria from the selected model for Kashkan compared to the other sub-catchments suggests that longer data will be needed for better modelling of catchments with higher variability of precipitation.
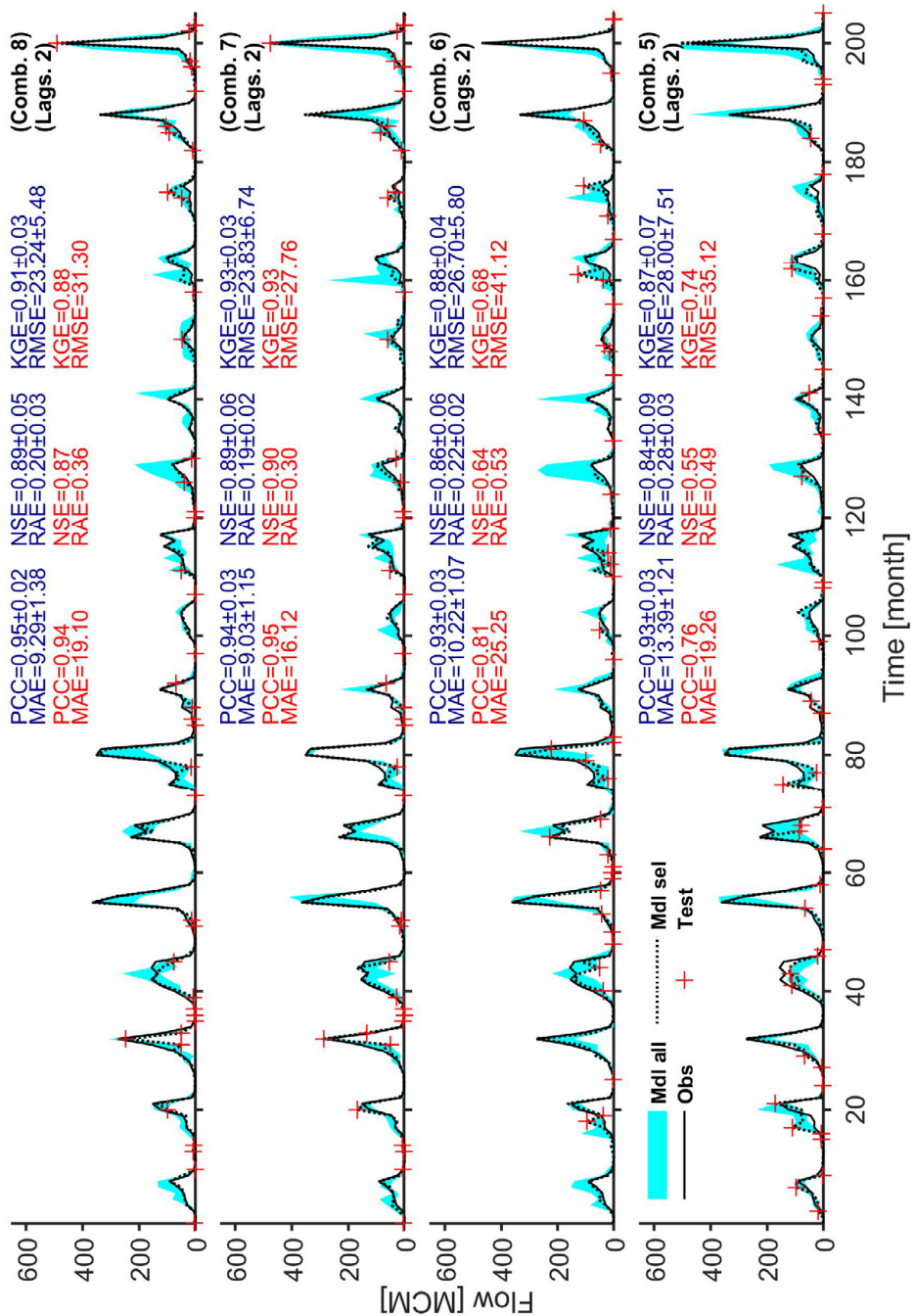
Figure 22. Observed (Obs) and modelled (Mdl) monthly runoff from Gamasiab sub-catchment for the combination of input variables (Comb.) and maximum lag times (Lags.) including the selected model (Mdl sel) and all models (Mdl all) of the 5-fold process. The performance values in blue are calculated using all data partitions for Mdl all. The performance values in red are calculated using the testing partition (Test) of Mdl sel.
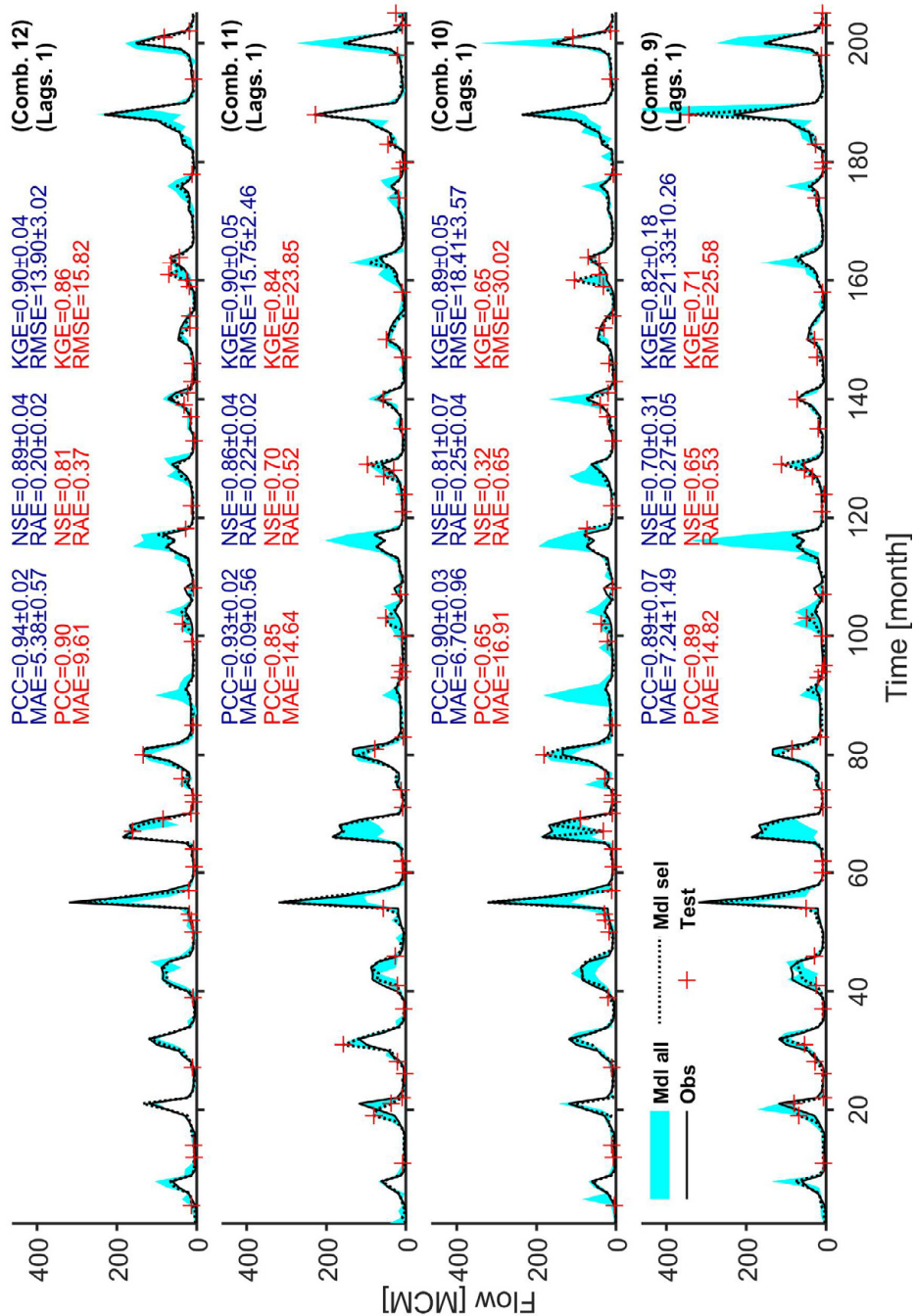
Figure 23. Observed (Obs) and modelled (Mdl) monthly runoff from Qarasu sub-catchment for the combination of input variables (Comb.) and maximum lag times (Lags.) including the selected model (Mdl sel) and all models (Mdl all) of the 5-fold process. The per-formance values in blue are calculated using all data partitions for Mdl all. The performance values in red are calculated using the testing partition (Test) of Mdl sel.

Figure 24. Observed (Obs) and modelled (Mdl) monthly runoff from Seymareh sub-catchment for the combination of input variables (Comb.) and maximum lag times (Lags.) including the selected model (Mdl sel) and all models (Mdl all) of the 5-fold process. The performance values in blue are calculated using all data partitions for Mdl all. The performance values in red are calculated using the testing partition (Test) of Mdl sel.

69
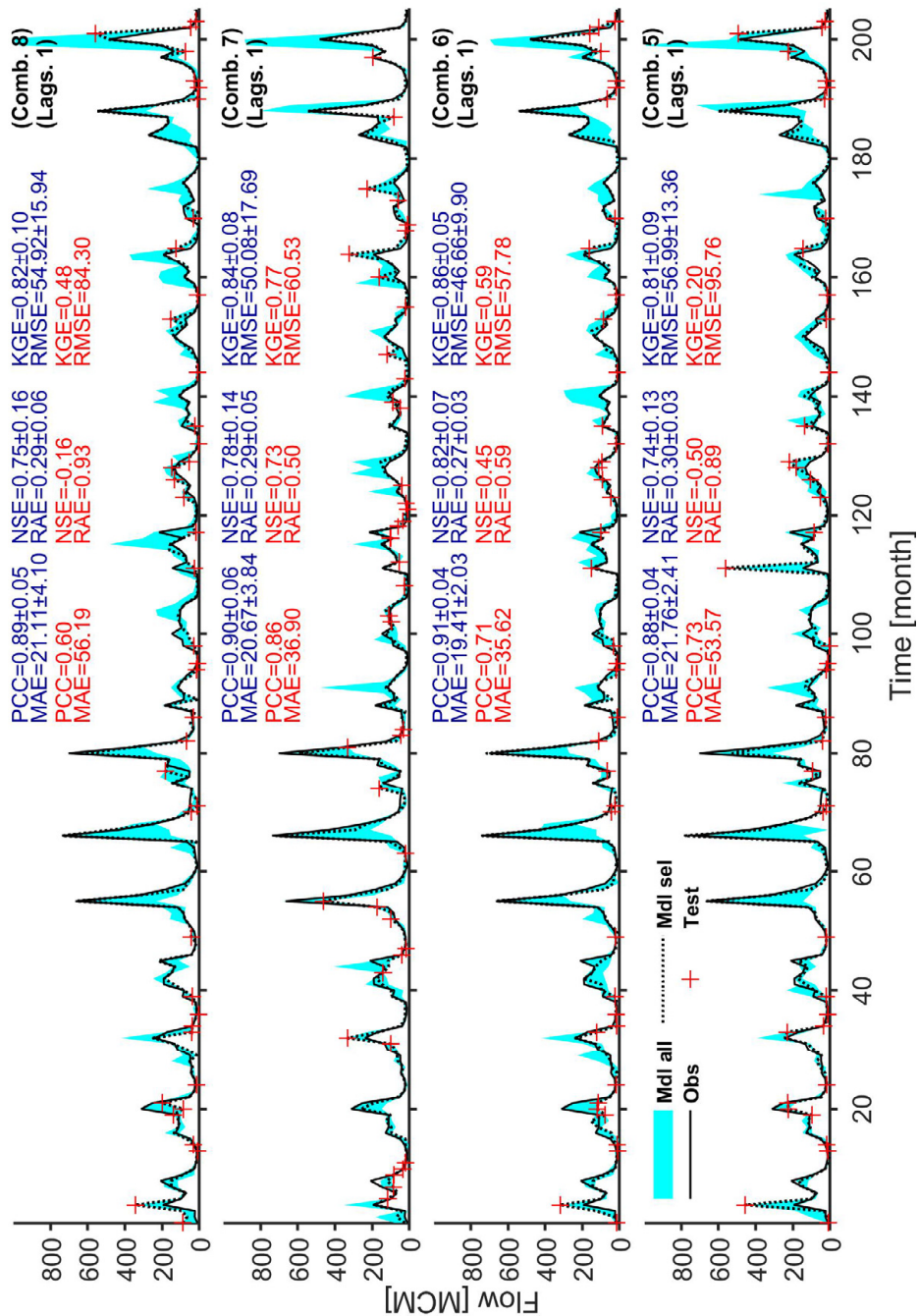
Figure 25. Observed (Obs) and modelled (Mdl) monthly runoff from Kashkan sub-catchment for the combination of input variables (Comb.) and maximum lag times (Lags.) including the selected model (Mdl sel) and all models (Mdl all) of the 5-fold process. The performance values in blue are calculated using all data partitions for Mdl all. The performance values in red are calculated using the testing partition (Test) of Mdl sel.
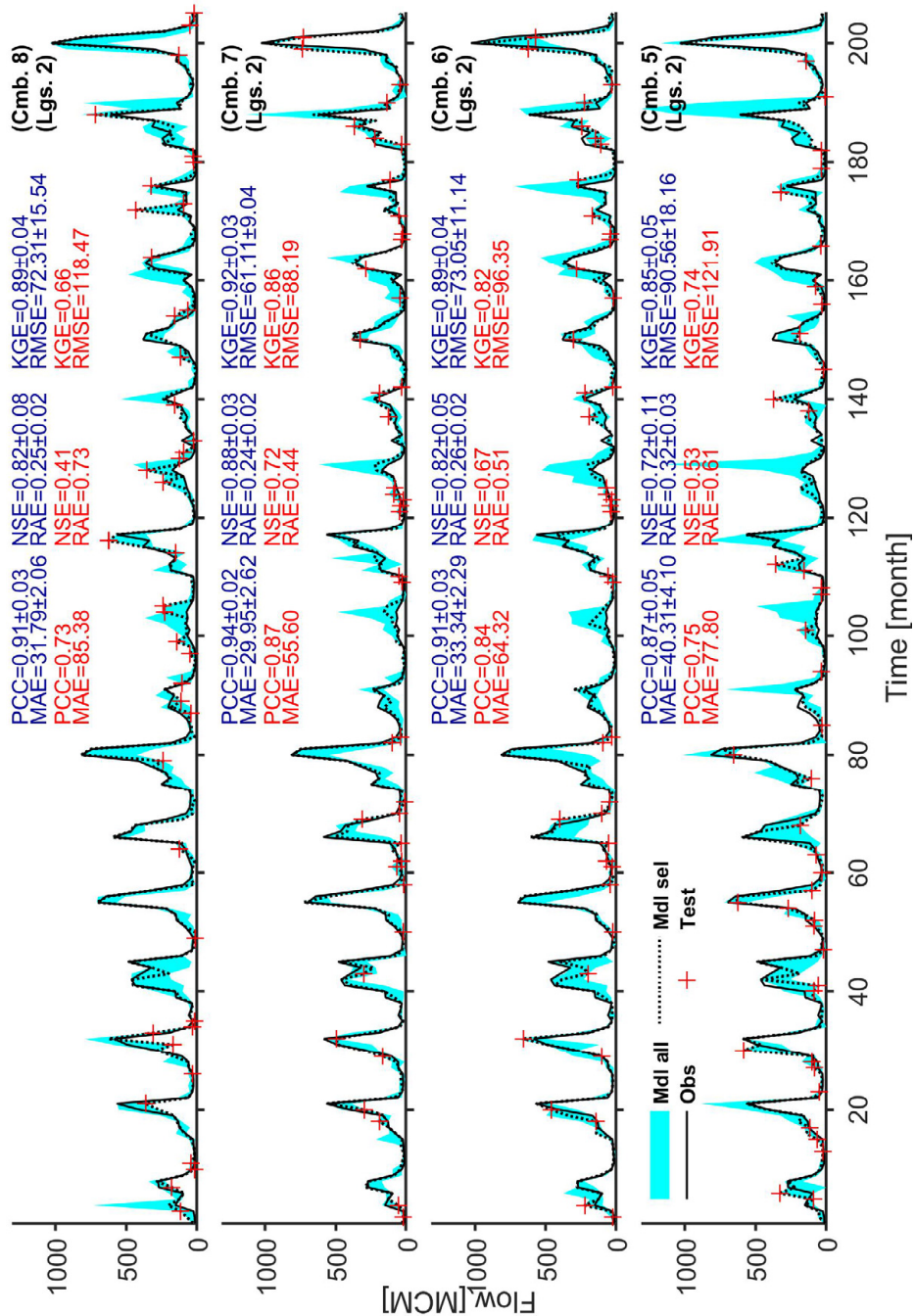
Figure 26. Observed (Obs) and modelled (Mdl) monthly runoff of the Karkheh reservoir for the combination of input variables (Comb.) and maximum lag times (Lags.) including the selected model (Mdl sel) and all models (Mdl all) of the 5-fold process. The performance values in blue are calculated using all data partitions for Mdl all. The performance values in red are calculated using the testing partition (Test) of Mdl sel.
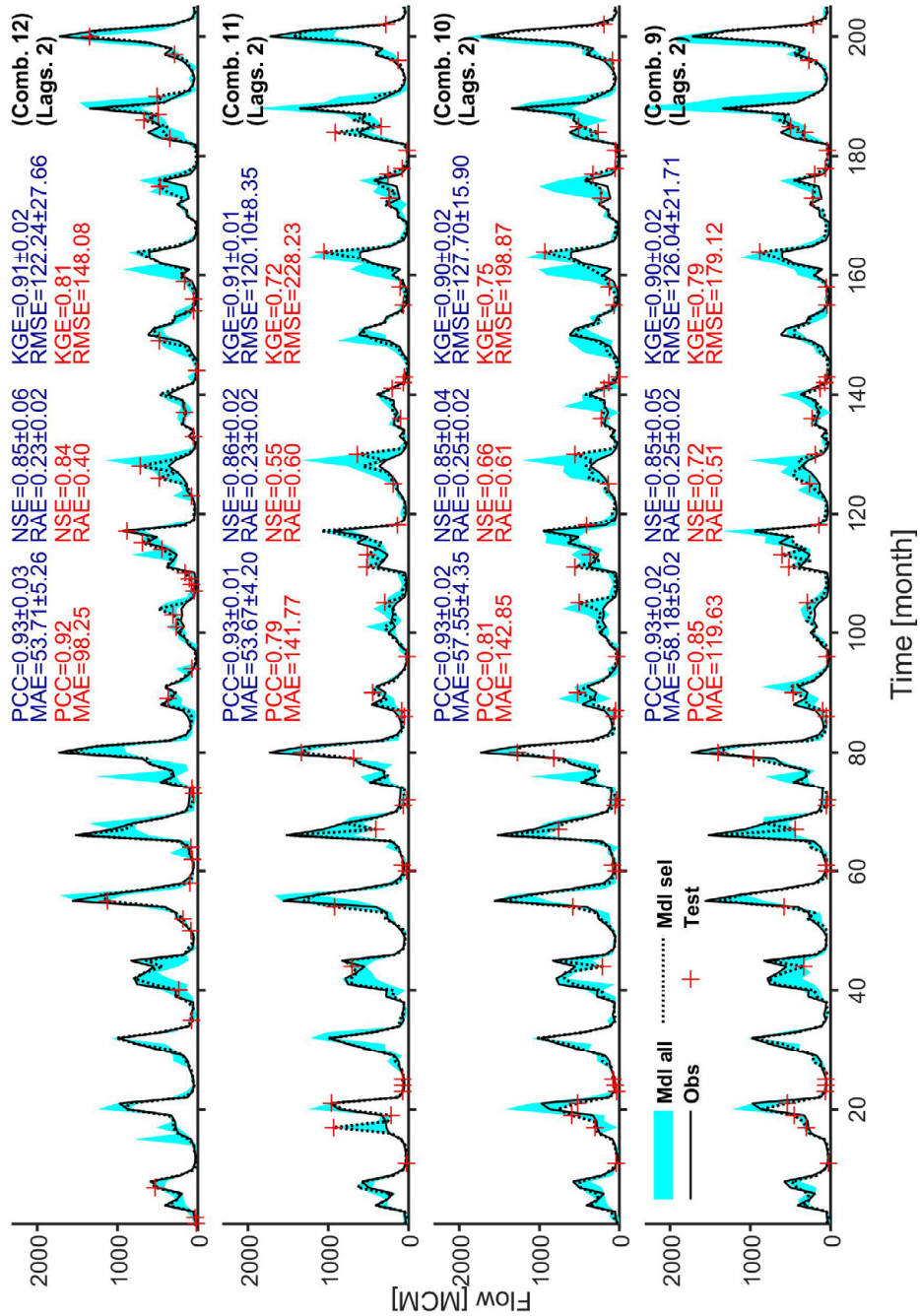
71

The suitability of IMERG products for runoff simulation is presented in different regions. In a study of a catchment in Brazil, Amorim et al. (2020) indicated that the IMERG-Final product could outperform the rain gauge and TRMM-TMPA product for monthly runoff simulation with a lower uncertainty. Higher-resolution implementation of GPM-IMERG products, such as hourly streamflow simulations by Zhu et al. (2021) in a subtropical monsoon climate of China, showed an overall acceptance of IMERG-Early, IMERG-Late, and TMPA 3B42RT for streamflow simulations. They showed that IMERG-Final overestimated low flows while performing the best for flood events. More interestingly, the satellite products could perform better than gauge-based data in detecting the peak flood time.

The general hypothesis for calculating the areal coverage ratios of precipitation was that not only the average precipitation over the catchment but also its spatial distribution contributes to the runoff variation. This was reasonable to assume but it is important to note that CCOVs and ECOVs do not directly explain the location of precipitation. Instead, they consider the areal coverage ratios of precipitation with a possible correlation with the spacetime patterns of precipitation. For example, the underlying stratiform, rather than convective/orographic, precipitation events (typically representing slight to moderate intensities of precipitation over larger areas and durations) can be reflected as a bigger coverage ratio (close to 1) at a few low precipitation categories (e.g., CCOV1 = 0.9 and CCOV2 = 0.8 while CCOV9 = 0 and CCOV10 = 0). Conversely, the underlying convective precipitation events (typically representing local but intense rains) can be reflected as a lower coverage ratio at a few higher precipitation categories (e.g., CCOV1 = 0 and CCOV2 = 0 while CCOV9 = 0.2 and CCOV10 = 0.1). Thus, CCOVs and ECOVs are only considered as additional inputs to DD models that can indirectly compensate for the lack of input data variability, that challenges lumped precipitation–runoff modelling. Anyway, these new variables were successful in all the studied catchments based on all the six performance criteria values. Thus, most likely, they can be useful in other study areas as well since they were formulized as catchment-specific and event-specific ratios. Some variation, such as a different categorization of precipitation data, might be needed depending on, e.g., how big the catchment is, how wet the climate is, and how long the available observation data are. For example, ECOVs contained six event-dependant variables, while CCOVs were based on ten catchment-specific categories, and the ECOVs were to some extent more useful than the CCOVs. The reason could be related to the presence of a small variation per a higher number of categories for training when the record is short. How long data should be used can also depend on the variability of the dataset.

A similar methodological variation can be imagined for the adjusted cross-validation and verification process, although the general idea can be as that was used here. For example, the larger testing portion for a 5-fold process (than for a 10-fold process) could help to ensure the robustness of the developed model in future uses. A 10-fold process, however, allows more data in calibration that could result in a

better training. Therefore, a reasonable strategy can be to first use the 5-fold process and then, depending on if the calibration needs improvement, the 10-fold process could also be additionally evaluated.

6 Conclusions

Ground validation of satellite precipitation (Paper I)

Although satellite-based precipitation products have been providing valuable data for the last few decades, studies have shown that there are some discrepancies between the satellite and ground-based precipitation data that require thorough validations. In this study, the performance of GPM IMERG products was evaluated in daily (Early, Late, and Final) and monthly temporal resolution using a well-maintained rain gauge network over the entire Iran country during the 2014-2017 period. Eight criteria indices were considered to evaluate the performance of IMERG products considering temporal and geospatial features. The general performance of the IMERG products against rain gauges approved the major improvement in the accuracy from IMERG Early to Final. In particular, the results showed a considerable decrease in rBIAS from IMERG Early to Final. The Q-Q plots analysis was carried out to evaluate the statistical distribution of satellite products versus rain gauge measurements. The findings revealed that the IMERG Final may not be the best choice for studying extreme events in the country, but the IMERG-Early and Late can do better. Investigation of the relationship between various physical and location-specific factors of rainfall showed that the increase in rainfall index (from dry to wet regions) leads to a lower and higher frequency of overestimations and underestimations, respectively. In addition, higher values of FAR were observed for most of the dry areas. The higher POD were more frequent in dry regions (perhaps due to the existence of many zero values) while lower POD values were observed in the wet regions. In general, the accuracy of the products increased from IMERG-Early to Final with an exception for extreme rainfall. As these analyses and results were conducted at the country level, it is suggested to validate the IMERG products at catchment scale before their extensive application.

Evaluating QPE by X-WR (Papers II and IV)

Regarding a single X-WR validation in southern Sweden, it was shown that the estimation of high-intensity rainfall was subject to attenuation due to heavy rain so that gathering of data was practically interrupted, especially at ranges longer than 20 km. For the two investigated rainfall events, overshooting of the lower-lying showers by the higher-level scans of radar (i.e., elevation angles 8 and 10°) caused huge underestimation at ranges as long as 19–30 km. On the other hand, rainfall

estimation at short ranges (<1 km), especially by lower-level scans (i.e., elevation angles 2 and 4°), was found to suffer from reflectivity contamination due to moving objects in the radar vicinity, resulting in overestimation. The results of this study showed that the rainfall estimation by the X-WR in mid-range (~5–10 km) was the most accurate as it was less affected by reflectivity contamination, overshooting, and attenuation due to heavy rain. All in all, higher resolution spatiotemporal rainfall monitoring for wider applications will benefit from the integration of data by a network of X-band WRs, assuming that deficiencies of individual radars can be overcome by a system of radars. Due to the various sources of error affecting rainfall estimation by radar, however, data-cleaning is not a straightforward task and will require detailed studies distinguishing between the affecting sources, according to the characteristics of the areal rainfall in time and space. Therefore, more investigations are needed that can combine data of different sources to improve estimation methods. An interesting prospect mentioned above is to use local X-band data to improve the quality of the national C-band WR-based products, that way producing an added value also outside the X-band domain.

Due to inconsistent rainfall estimation by single-device X-WR operation, varying with the radar range and elevation angle level, a merging X-WR framework emphasising the role of range and level was designed and tested using neural network and regression models.

In summary, the study aimed to merge data from two X-WRs in southern Sweden for better rainfall estimations in their overlapping coverage area. The X-WRs in Dalby and Helsingborg operated at 50 and 70 km ranges and scanned the weather at five elevation angles (1.5, 2, 4, 6, and 8°) and one elevation angle (2°) per minute during May-September 2021, respectively. Each scan of an X-WR provided a full range data map of the radar variables (RHOHV, KDP, VRAD, DBZH, and ZDR that were used in the merging models) as well as a built-in rainfall intensity product (RATE based on the Marshall–Palmer equation adjusted for attenuation correction). The overlapping coverage of the X-WRs encompassed 38 tipping bucket rain gauges, which were used as ground truth for calibration and validation of two merging models after some preliminary steps, and to assure the generalization of the models and efficient reduction of the data processing time. Thus, the gauge-detected rainfall events were extracted for the study area and those with the MGI of 2 mm h^{-1} or less (based on the 30-min accumulations) were excluded from the study. Radar data were downloaded for the studied events and some extra events had to be removed due to the missing X-WR data. The study area was divided into some sub-areas where four of them included all 38 gauges (Zone I-IV). For merging the X-WRs data, the artificial neural networks (ANN) and Marshall–Palmer type linear regression-based model (RMP) were calibrated based on major part of the data

(training and in-process validation for ANN). The calibration was repeated 6000 times to find the optimum ANN architecture and prevent a parameterization stuck in local minima. Finally, four rainfall estimation models equivalent to the number of zones were developed for each modelling type (ANN and RMP).

Based on 20-25% of the data, which were kept out of the calibration of ANN and RMP, additional verifications were considered. As a result, the 5-min rainfall estimation was obviously improved over most of the overlapping area by merging the two X-WRs. Since the XRs' software makes it possible to change the operational range from 50 km to 70 km, it is, therefore, recommended to do so for the Dalby XR to increase the overlapping area in the future. However, the accuracy of the rainfall estimations (also the estimated quantiles) of the single level RATEs and merging models, ANN and RMP, were not interesting in Zone III. This zone was the farthest to Dalby and closest to the Helsingborg X-WR. In our study, data from only one level of Helsingborg X-WR was available at 2° elevation angle. This level of the Helsingborg X-WR and the lower levels from Dalby X-WR showed to be the most erroneous levels for some of the zones perhaps due to the higher ground clutter chance at lower altitude scans. Due to a recent adjustment, more levels are now available from the Helsingborg X-WR, and it is expected that this will help to improve the rainfall estimation for the entire coverage in future studies. As noted earlier, the X-WRs susceptibility to errors such as attenuation, overshooting, and ground clutter depended on radar range and level. Also, the underlying causes of the inconsistency in single-level radar scans could depend on the storm characteristics that are usually reflected in vertical profile of storm (convective vs. stratiform). Therefore, the hybrid approach of the study for merging X-WRs emphasised the role of range and level. Since the nature of these dependencies could be complex and non-linear, the use of AI modelling such as ANN was suggested and proved useful. The generalized ANN approach employed in the study showed no sign of overfitting (confirmed by comparing with RMP and RATEs during testing periods which were not used in calibration). Also, it showed at least as good as RMP with some better performance for representing most extreme values.

A limitation due to the use of tipping buckets in the study was that the developed models had to be calibrated at 5-min scale rather than the original 1-min data for the radars. Using coarser scales such as 10 min could lower the uncertainties of the calibration but would be less interesting for urban runoff modelling, which can vary substantially in 1-2 min scales. This then may suggest the need for alternative ground truth data such as disdrometers or higher precision rain-gauges. Recently

three disdrometers and a vertically oriented Micro Rain Radar were added to the overlapping coverage of the two X-WRs and can help to increase the temporal resolution of the ground-truth and merging products, among others. The study indicated high potential for such improvements based on the designed data-driven approaches for merging X-WRs.

Satellite-based monthly runoff estimation using ANN (Paper III)

The new input variables were formulated based on the gridded RS-based data, primarily useful for large-scale runoff modelling in sparsely gauged catchments. The combination of these variables with simple hydrological notions were put into a new conceptualized AI-assisted data-driven (DD) framework. Backpropagation feed-forward ANNs, widely used in hydrological modelling, was used as the reference DD model. Each of the employed input–output combinations were evaluated using an adjusted cross-validation and verification process to minimize overfitting. To assure achieving outputs with a reliable degree of generalization, many network configurations were evaluated for each combination of input–output variables. Eventually, multiple hybrid models from the best-ranked single models were selected for five case studies of the KRB with different catchment sizes between 5,000 and 43,000 km^2. As a result, the best runoff model for all catchments relied on an input variable combination that incorporated ECOVs (or both CCOVs and ECOVs) together with reference input variable combinations. From the inter-catchment comparison, it was shown that, regardless of the catchment size, the best and worst performance criteria were obtained for Gamasiab and Kashkan, having the lowest and the highest spacetime precipitation variation, respectively. More interestingly, for Kashkan, the improvement of the performance scores by incorporating the precipitation coverage ratios, compared to the condition without the coverage ratios, was the highest among all sub-catchments. However, the performance of modelling in Kashkan showed a higher dependency on the data portions used for calibration and verification. Thus, while the highest usefulness (from test data) was observed for the most challenging catchment in the sense that it had the highest variability of precipitation, a longer data length would be needed for generally better-performing model development in such catchments. On the contrary, the lowest degree of usefulness was for the largest catchment area, the entire study area of Karkheh.

In conclusion, the shown usefulness of areal precipitation coverage-based variables here suggests new conceptualization potentials to leverage the increasingly advancing DD methods and satellite RS data in rainfall–runoff modelling, along with the use of physically-based (or conceptual) models. One of the strengths of AI-assisted DD modelling, such as ANN algorithms, is the ability to combine different inputs and apply multiple time lags with the automatization of modelling under a different architecture, which is not often the case for regular hydrological modelling.

In addition, physically based (or conceptual) modelling is not an ideal tool for the direct simulation of monthly runoff as its underlying concepts such as the UH theory is usually built to relate precipitation and runoff data at an event scale. Thus, the monthly runoff estimates are accumulated, e.g., from the initial daily estimates. These issues may result in computationally expensive modelling using regular physically based (or conceptual) hydrological models when large-scale simulations need to evolve in accordance with the advancing worldwide satellite observations.

Finally, as in any hydrological study relying on indirect estimations and modelling, the methodology introduced here is subject to uncertainty. Probably, the most important aspect is related to the limited length of the datasets for the advanced, high-resolution, satellite data. There are obvious benefits of the new input variables used here; however, reliance on the model as well depends on the long-term representativity of the data. Developing a model using available data may still be useful for locations without an alternative that is a valid situation for many data-scarce catchments. As a technical note, the practical application of the modelling as described here can result in an error when the observed catchment-scale precipitation (P) in a month is greater than the higher edge of the final category of P for a catchment, and the model relies on CCOVs. To avoid such errors, the higher edge of the final category should be monitored. Another issue is related to the RS-based input variables used in the study, as well as the selection of what satellite product to use. The GPM is an advanced satellite precipitation mission that has gained interest in recent research of satellite precipitation after its precursor TRMM. GPM-IMERG data are now expanded to almost the same time span as its precursor and presented in a few products at different temporal resolutions and data access latencies. Deciding which of the IMERG-Final or IMERG-Late products (probably the most useful ones here) is better to use for a region needs thorough investigations. As we discussed in the Introduction, the RS data are subject to errors, but it is not a straightforward task to adjust the biased data using the usually sparse ground observations, particularly in data-scarce catchments that will perhaps benefit most from the methodology.

This study focused on monthly runoff modelling and used monthly input variables. The benefits of using direct monthly data for strategic surface water management were discussed in the previous paragraph. However, daily data are also interesting for other purposes where, for example, sub-monthly data are important. It has been noted that the methodology introduced here needs more investigations. Additionally, it is worth mentioning that some of the RS-based inputs used in this study (e.g., ET) were only available at 8-day and 16-day resolutions (at highest) that may not be favourable for daily modelling.

Future scopes

From the above conclusions about satellite and radar precipitation data, it seems RS- and AI-assisted models are useful for more reliable hydrological applications in the

future. Therefore, more studies can be conducted to evaluate other variations of the methodology (e.g., other machine learning models, etc.). A challenge regarding the calibration of the RS data, however, is incomparable scales of the ground-truth and RS data. Also, the efficacy of ground-truth data can be questioned, e.g., when the RS data are only calibrated at a few grids/bins from a local relationship obtained based on sparse in-situ rain gauges. Therefore, a fundamental step to improve the applications of the AI and RS data is to increase the in-situ data or use different calibration sources such as runoff. For example, a simple method could be based on using rain gauges and RS data together. Then, the calibration can be obtained based on the runoff response as a more applied output. Future studies can combine different satellite sensors and radar types with those used here. Also, they can use longer records of satellite data which seems necessary for catchments with higher variability of precipitation (Paper III). Also, the merging of X-WR data can be based on the longer observations where, e.g., each season or month can have its own merging model. Also, the methodologies can be extended to forecast problems. Then, the use of recurrent neural networks, e.g., can be useful.

References

Amorim JD, Viola MR, Junqueira R, et al. (2020) Evaluation of Satellite Precipitation Products for Hydrological Modeling in the Brazilian Cerrado Biome. *Water* 12(9).

Antonini A, Melani S, Corongiu M, et al. (2014) Radar Networking over the Tyrrenian Sea. *Proceedings of the 8th European Conference on Radar in Meteorology and Hydrology ERAD.*

Antonini A, Melani S, Corongiu M, et al. (2017) On the implementation of a regional X-band weather radar network. *Atmosphere* 8(2): 25.

Asong Z, Razavi S, Wheater H, et al. (2017) Evaluation of Integrated Multisatellite Retrievals for GPM (IMERG) over southern Canada against ground precipitation observations: A preliminary assessment. *Journal of hydrometeorology* 18(4): 1033-1050.

Austin GL and Austin LB (1974) The use of radar in urban hydrology. *Journal of hydrology* 22(1-2): 131-142.

Becker A, Finger P, Meyer-Christoffer A, et al. (2013) A description of the global land-surface precipitation data products of the Global Precipitation Climatology Centre with sample applications including centennial (trend) analysis from 1901–present. *Earth System Science Data* 5(1): 71-99.

Beria H, Nanda T, Singh Bisht D, et al. (2017) Does the GPM mission improve the systematic error component in satellite rainfall estimates over TRMM? An evaluation at a pan-India scale. *Hydrology and Earth System Sciences* 21(12): 6117-6134.

Berne A and Krajewski WF (2013) Radar for hydrology: Unfulfilled promise or unrecognized potential? *Advances in Water Resources* 51: 357-366.

Bringi VN and Chandrasekar V (2001) *Polarimetric Doppler weather radar: principles and applications.* Cambridge university press.

Browning K (1978) Meteorological applications of radar. *Reports on progress in physics* 41(5): 761.

Büyükbas E (2009) Assess the Current and Potential Capabilities of Weather Radars for the Use in WMO Integrated Global Observing System (WIGOS). *Proceedings of the Joint Meeting of the CIMO Expert Team on Remote Sensing Upper-air Technology and Techniques and CBS Expert Team on Surface Based Remote Sensing, Geneva, Switzerland.* 23-27.

Chandrasekar V, Wang Y and Chen H (2012) The CASA quantitative precipitation estimation system: a five year validation study. *Natural Hazards and Earth System Sciences* 12(9): 2811-2820.

Chen S, Hong Y, Gourley JJ, et al. (2013) Evaluation of the successive V6 and V7 TRMM multisatellite precipitation analysis over the Continental United States. *Water Resources Research* 49(12): 8174-8186.

Chu D (2018) MODIS remote sensing approaches to monitoring soil moisture in Tibet, China. *Remote Sensing Letters* 9(12): 1148-1157.

Delrieu G, Berne A, Borga M, et al. (2009) Weather radar and hydrology. *Advances in Water Resources* 7(32): pp 969-974.

Didan K, Munoz AB, Solano R, et al. (2015) MODIS vegetation index user's guide (MOD13 series). *University of Arizona: Vegetation Index and Phenology Lab*.

Doviak RJ and Dušan SZ (2006) *Doppler radar and weather observations.* Mineola, New York: Dover Publications, Inc.

Einfalt T (2003) A user perspective in Germany: What is expected by agencies and government from radar data? *International Journal of River Basin Management* 1(3): 199-203.

Einfalt T, Arnbjerg-Nielsen K, Golz C, et al. (2004) Towards a roadmap for use of radar rainfall data in urban drainage. *Journal of hydrology* 299(3-4): 186-202.

Ensor LA and Robeson SM (2008) Statistical characteristics of daily precipitation: comparisons of gridded and point datasets. *Journal of Applied Meteorology and Climatology* 47(9): 2468-2476.

Foelsche U, Kirchengast G, Fuchsberger J, et al. (2017) Evaluation of GPM IMERG Early, Late, and Final rainfall estimates using WegenerNet gauge data in southeastern Austria. *Hydrology and Earth System Sciences* 21(12): 6559-6572.

Frei C (2014) Interpolation of temperature in a mountainous region using nonlinear profiles and non-Euclidean distances. *International Journal of Climatology* 34(5): 1585-1605.

Furcolo P, Pelosi A and Rossi F (2016) Statistical identification of orographic effects in the regional analysis of extreme rainfall. *Hydrological Processes* 30(9): 1342-1353.

Gadelha AN, Coelho VHR, Xavier AC, et al. (2019) Grid box-level evaluation of IMERG over Brazil at various space and time scales. *Atmospheric Research* 218: 231-244.

Gires A, Onof C, Maksimovic C, et al. (2012) Quantifying the impact of small scale unmeasured rainfall variability on urban runoff through multifractal downscaling: A case study. *Journal of hydrology* 442: 117-128.

Goormans T and Willems P (2013) Using local weather radar data for sewer system modeling: case study in Flanders, Belgium. *Journal of Hydrologic Engineering* 18(2): 269-278.

Gottardi F, Obled C, Gailhard J, et al. (2012) Statistical reanalysis of precipitation fields based on ground network data and weather patterns: Application over French mountains. *Journal of hydrology* 432: 154-167.

Hagan MT, Demuth HB and Beale M (1997) *Neural network design.* PWS Publishing Co.

Han D, Cluckie ID, Griffith RJ, et al. (2000) Using weather radars to measure rainfall in urban catchments. *Journal of Urban Technology* 7(1): 85-102.

Hari V, Rakovec O, Markonis Y, et al. (2020) Increased future occurrences of the exceptional 2018–2019 Central European drought under global warming. *Scientific Reports* 10(1): 1-10.

Harrold T (1965) Meteorological Office Scientific Paper. London: HMSO.

Hashemi H, Fayne J, Lakshmi V, et al. (2020) Very high resolution, altitude-corrected, TMPA-based monthly satellite precipitation product over the CONUS. *Scientific data* 7(1): 1-10.

Hashemi H, Nordin M, Lakshmi V, et al. (2017) Bias correction of long-term satellite monthly precipitation product (TRMM 3B43) over the conterminous United States. *Journal of hydrometeorology* 18(9): 2491-2509.

Hiebl J and Frei C (2018) Daily precipitation grids for Austria since 1961—Development and evaluation of a spatial dataset for hydroclimatic monitoring and modelling. *Theoretical and Applied Climatology* 132(1): 327-345.

Hofierka J, Parajka J, Mitasova H, et al. (2002) Multivariate interpolation of precipitation using regularized spline with tension. *Transactions in GIS* 6(2): 135-150.

Hosseini SH (2019) Disastrous floods after prolonged droughts have challenged Iran. *FUF-bladet*, 17 juni, 2019, 30-32.

Hou AY, Kakar RK, Neeck S, et al. (2014) The global precipitation measurement mission. *Bulletin of the American Meteorological Society* 95(5): 701-722.

Houze Jr RA (2012) Orographic effects on precipitating clouds. *Reviews of Geophysics* 50(1).

Hsu K-l, Gao X, Sorooshian S, et al. (1997) Precipitation estimation from remotely sensed information using artificial neural networks. *Journal of Applied Meteorology and Climatology* 36(9): 1176-1190.

Huffman G, Bolvin D, Braithwaite D, et al. (2019) Algorithm Theoretical Basis Document (ATBD) Version 06: *NASA Global Precipitation Measurement (GPM) Integrated Multi-Satellite Retrievals for GPM (IMERG)*; NASA: Greenbelt, MD, USA.

Huffman GJ, Bolvin DT, Braithwaite D, et al. (2015) NASA global precipitation measurement (GPM) integrated multi-satellite retrievals for GPM (IMERG). *lgorithm Theoretical Basis Document (ATBD) Version* 4:26.

Huffman GJ, Bolvin DT, Nelkin EJ, et al. (2007) The TRMM multisatellite precipitation analysis (TMPA): Quasi-global, multiyear, combined-sensor precipitation estimates at fine scales. *Journal of hydrometeorology* 8(1): 38-55.

Jensen NE and Pedersen L (2005) Spatial variability of rainfall: Variations within a single radar pixel. *Atmospheric Research* 77(1): 269-277.

Joyce RJ, Janowiak JE, Arkin PA, et al. (2004) CMORPH: A method that produces global precipitation estimates from passive microwave and infrared data at high spatial and temporal resolution. *Journal of hydrometeorology* 5(3): 487-503.

Kessler E (1966) Radar measurements for the assessment of areal rainfall: Review and outlook. *Water Resources Research* 2(3): 413-425.

Khodadoust Siuki S, Saghafian B and Moazami S (2017) Comprehensive evaluation of 3-hourly TRMM and half-hourly GPM-IMERG satellite precipitation products. *International Journal of Remote Sensing* 38(2): 558-571.

Kidd C, Becker A, Huffman GJ, et al. (2017) So, how much of the Earth's surface is covered by rain gauges? *Bulletin of the American Meteorological Society* 98(1): 69-78.

Kidd C and Levizzani V (2011) Status of satellite precipitation retrievals. *Hydrology and Earth System Sciences* 15(4): 1109-1116.

Krajewski W and Smith JA (2002) Radar hydrology: rainfall estimation. *Advances in Water Resources* 25(8-12): 1387-1394.

Krajewski WF, Villarini G and Smith JA (2010) Radar-rainfall uncertainties: Where are we after thirty years of effort? *Bulletin of the American Meteorological Society* 91(1): 87-94.

Krämer S and Verworn H-R (2009) Improved radar data processing algorithms for quantitative rainfall estimation in real time. *Water Science and Technology* 60(1): 175-184.

Kumar TVL, Barbosa HA, Thakur MK, et al. (2019) Validation of satellite (TMPA and IMERG) rainfall products with the IMD gridded data sets over monsoon core region of India. *Satellite Information Classification and Interpretation*. IntechOpen.

Kumjian, M. R., 2013: Principles and applications of dual-polarization weather radar. Part I: Description of the polarimetric radar variables. *Journal of Operational Meteorology* 1(19), 226-242.

Lengfeld K, Clemens M, Münster H, et al. (2013) PATTERN: Advantages of high-resolution weather radar networks. *Proceedings of American Meteorological Society 36th Conference on Radar Meteorology, Breckenridge, CO, USA.* 16-20.

Lengfeld K, Clemens M, Münster H, et al. (2014) Performance of high-resolution X-band weather radar networks–the PATTERN example. *Atmospheric Measurement Techniques* 7(12): 4151-4166.

Liu J and Niyogi D (2019) Meta-analysis of urbanization impact on rainfall modification. *Scientific Reports* 9(1): 1-14.

Liu X, Yang T, Hsu K, et al. (2017) Evaluating the streamflow simulation capability of PERSIANN-CDR daily rainfall products in two river basins on the Tibetan Plateau. *Hydrology and Earth System Sciences* 21(1): 169-181.

Marshall JS and Palmer WMcK (1948) The distribution of raindrops with size. *J. meteor.* 5: 165-166.

Meischner P (2005) *Weather radar: principles and advanced applications.* Springer Science & Business Media.

Mergili M and Kerschner H (2015) Gridded precipitation mapping in mountainous terrain combining GRASS and R. *Norsk Geografisk Tidsskrift-Norwegian Journal of Geography* 69(1): 2-17.

Michaelides SC (2008) Precipitation: Advances in measurement, estimation and prediction. Springer Science & Business Media.

Mishra KV, Krajewski WF, Goska R, et al. (2016) Deployment and performance analyses of high-resolution Iowa XPOL radar system during the NASA IFloodS campaign. *Journal of hydrometeorology* 17(2): 455-479.

Mo C, Zhang M, Ruan Y, et al. (2020) Accuracy Analysis of IMERG Satellite Rainfall Data and Its Application in Long-term Runoff Simulation. *Water* 12(8): 2177.

Mondal A, Lakshmi V and Hashemi H (2018) Intercomparison of trend analysis of multisatellite monthly precipitation products and gauge measurements for river basins of India. *Journal of hydrology* 565: 779-790.

Moustakis Y, Onof CJ and Paschalis A (2020) Atmospheric convection, dynamics and topography shape the scaling pattern of hourly rainfall extremes with temperature globally. *Communications Earth & Environment* 1(1): 1-9.

Musie M, Sen S and Srivastava P (2019) Comparison and evaluation of gridded precipitation datasets for streamflow simulation in data scarce watersheds of Ethiopia. *Journal of hydrology* 579: 124168.

Myhre G, Alterskjær K, Stjern CW, et al. (2019) Frequency of extreme precipitation increases extensively with event rareness under global warming. *Scientific Reports* 9(1): 1-10.

Omranian E and Sharif HO (2018) Evaluation of the global precipitation measurement (GPM) satellite rainfall products over the lower Colorado River basin, Texas. *JAWRA Journal of the American Water Resources Association* 54(4): 882-898.

Orlanski I (1975) A rational subdivision of scales for atmospheric processes. *Bulletin of the American Meteorological Society* 56(5): 527-530.

Pedersen L, Jensen NE and Madsen H (2008) Estimation of radar calibration uncertainties related to the spatial variability of rainfall within a single radar pixel—statistical analysis of rainfall data from a dense network of rain gauges. *World Environmental and Water Resources Congress 2008: Ahupua'A.* 1-10.

Pedersen L, Jensen NE and Madsen H (2010) Calibration of Local Area Weather Radar—Identifying significant factors affecting the calibration. *Atmospheric Research* 97(1-2): 129-143.

Rana S, McGregor J and Renwick J (2015) Precipitation seasonality over the Indian subcontinent: An evaluation of gauge, reanalyses, and satellite retrievals. *Journal of hydrometeorology* 16(2): 631-651.

Roca R, Chambon P, Jobard I, et al. (2010) Comparing satellite and surface rainfall products over West Africa at meteorologically relevant scales during the AMMA campaign using error estimates. *Journal of Applied Meteorology and Climatology* 49(4): 715-731.

Rollenbeck R and Bendix J (2006) Experimental calibration of a cost-effective X-band weather radar for climate ecological studies in southern Ecuador. *Atmospheric Research* 79(3-4): 296-316.

Running SW, Mu Q, Zhao M, et al. (2019) MODIS Global Terrestrial Evapotranspiration (ET) Product (MOD16A2/A3 and Year-End Gap-Filled MOD16A2GF/A3GF) NASA Earth Observing System MODIS Land Algorithm (For Collection 6). NASA: Washington, DC, USA.

Schellart A, Liguori S, Krämer S, et al. (2014) Comparing quantitative precipitation forecast methods for prediction of sewer flows in a small urban area. *Hydrological Sciences Journal* 59(7): 1418-1436.

Schellart ANA, Shepherd WJ and Saul AJ (2012) Influence of rainfall estimation error and spatial variability on sewer flow prediction at a small urban scale. *Advances in Water Resources* 45: 65-75.

Shah S, Notarpietro R and Branca M (2015) Storm Identification, Tracking and Forecasting Using High-Resolution Images of Short-Range X-Band Radar. *Atmosphere* 6(5): 579-606.

Sharif HO, Mahmoud MT and Al-Zahrani M (2018) Performance of Different Global Precipitation Measurement IMERG Satellite Products over Saudi Arabia. *AGU Fall Meeting Abstracts.* H43F-2476.

Sharif HO and Ogden FL (2014) Mass-conserving remapping of radar data onto two-dimensional cartesian coordinates for hydrologic applications. *Journal of hydrometeorology* 15(6): 2190-2202.

Sharifi E, Steinacker R and Saghafian B (2016) Assessment of GPM-IMERG and Other Precipitation Products against Gauge Data under Different Topographic and Climatic Conditions in Iran: Preliminary Results. *Remote Sensing* 8(2): 135.

Smith JA, Baeck ML, Meierdiercks KL, et al. (2007) Radar rainfall estimation for flash flood forecasting in small urban watersheds. *Advances in Water Resources* 30(10): 2087-2097.

Smith JA and Krajewski WF (1991) Estimation of the mean field bias of radar rainfall estimates. *Journal of Applied Meteorology and Climatology* 30(4): 397-412.

Sun Q, Miao C, Duan Q, et al. (2018) A review of global precipitation data sets: Data sources, estimation, and intercomparisons. *Reviews of Geophysics* 56(1): 79-107.

Sungmin O and Kirstetter PE (2018) Evaluation of diurnal variation of GPM IMERG-derived summer precipitation over the contiguous US using MRMS data. *Quarterly Journal of the Royal Meteorological Society* 144: 270-281.

Tabari H (2020) Climate change impact on flood and extreme precipitation increases with water availability. *Scientific Reports* 10(1): 1-10.

Tan ML and Santo H (2018) Comparison of GPM IMERG, TMPA 3B42 and PERSIANN-CDR satellite precipitation products over Malaysia. *Atmospheric Research* 202: 63-76.

Tang G, Behrangi A, Long D, et al. (2018) Accounting for spatiotemporal errors of gauges: A critical step to evaluate gridded precipitation products. *Journal of hydrology* 559: 294-306.

Thorndahl S, Beven KJ, Jensen JB, et al. (2008) Event based uncertainty assessment in urban drainage modelling, applying the GLUE methodology. *Journal of hydrology* 357(3-4): 421-437.

Thorndahl S, Einfalt T, Willems P, et al. (2017) Weather radar rainfall data in urban hydrology. *Hydrology and Earth System Sciences* 21(3): 1359-1380.

Thorndahl S and Rasmussen MR (2012) Marine X-band weather radar data calibration. *Atmospheric Research* 103: 33-44.

Tilford K, Fox N and Collier C (2002) Application of weather radar data for urban hydrology. *Meteorological Applications* 9(1): 95-104.

Trabal JM, Colom-Ustariz JG, Cruz-Pol SL, et al. (2012) Remote sensing of weather hazards using a low-cost and minimal infrastructure off-the-grid weather radar network. *IEEE Transactions on Geoscience and Remote Sensing* 51(5): 2541-2555.

Van de Beek C, Leijnse H, Hazenberg P, et al. (2016) Close-range radar rainfall estimation and error analysis. *Atmospheric Measurement Techniques* 9(8): 3837-3850.

Van de Beek C, Leijnse H, Stricker J, et al. (2010) Performance of high-resolution X-band radar for rainfall measurement in The Netherlands. *Hydrology and Earth System Sciences* 14(2): 205-221.

Villarini G and Krajewski WF (2010) Review of the different sources of uncertainty in single polarization radar-based estimates of rainfall. *Surveys in geophysics* 31(1): 107-129.

Villarini G, Mandapaka PV, Krajewski WF, et al. (2008) Rainfall and sampling uncertainties: A rain gauge perspective. *Journal of Geophysical Research: Atmospheres* 113(D11).

Villarini G, Smith JA, Baeck ML, et al. (2010) Radar analyses of extreme rainfall and flooding in urban drainage basins. *Journal of hydrology* 381(3-4): 266-286.

Wagner PD, Fiener P, Wilken F, et al. (2012) Comparison and evaluation of spatial interpolation schemes for daily rainfall in data scarce regions. *Journal of hydrology* 464: 388-400.

Wang L, Qu J, Zhang S, et al. (2007) Soil moisture estimation using MODIS and ground measurements in eastern China. *International Journal of Remote Sensing* 28(6): 1413-1418.

Wang Z, Zhong R, Lai C, et al. (2017) Evaluation of the GPM IMERG satellite-based precipitation products and the hydrological utility. *Atmospheric Research* 196: 151-163.

Willems P (2001) Stochastic description of the rainfall input errors in lumped hydrological models. *Stochastic environmental research and risk assessment* 15(2): 132-152.

Wilson JW and Brandes EA (1979) Radar measurement of rainfall—A summary. *Bulletin of the American Meteorological Society* 60(9): 1048-1060.

Worqlul AW, Maathuis B, Adem AA, et al. (2014) Comparison of rainfall estimations by TRMM 3B42, MPEG and CFSR with ground-observed data for the Lake Tana basin in Ethiopia. *Hydrology and Earth System Sciences* 18(12): 4871-4881.

Xi Y and Liu G (2018) Evaluation of GPM Day-1 IMERG dataset with the point rain gauge records over the Netherlands and Sichuan province, China. *AGU Fall Meeting Abstracts.* H33I-2208.

Xu W, Zou Y, Zhang G, et al. (2015) A comparison among spatial interpolation techniques for daily rainfall data in Sichuan Province, China. *International Journal of Climatology* 35(10): 2898-2907.

Yang Y, Ren L, Wu M, et al. (2022) Abrupt emissions reductions during COVID-19 contributed to record summer rainfall in China. *Nature Communications* 13(1): 1-7.

Yuan J, Tilford K, Jiang H, et al. (1999) Real-time urban drainage system modelling using weather radar rainfall data. *Physics and Chemistry of the Earth, Part B: Hydrology, Oceans and Atmosphere* 24(8): 915-919.

Zhang Z, Tian J, Huang Y, et al. (2019) Hydrologic evaluation of TRMM and GPM IMERG satellite-based precipitation in a humid basin of China. *Remote Sensing* 11(4): 431.

Zhu Q, Zhou D, Luo Y, et al. (2021) Suitability of high-temporal satellite-based precipitation products in flood simulation over a humid region of China. *Hydrological Sciences Journal* 66(1): 104-117.